Chapter 4
GO/rGO as Advanced Materials for Energy Storage and Conversion

Gang Wu and Wei Gao

Abstract Recently, GO/rGO has become promising platforms for advanced materials in energy related technologies. Extensive applications of rGO have been explored in a variety of electrochemical energy storage and conversion technologies (e.g., fuel cells, metal–air batteries, supercapacitors, and water splitting devices). In particular, GO/rGO was studied as efficient components in catalysts in fuel cells and metal–air batteries for the oxygen reduction reaction (ORR) and oxygen evolution reaction (OER), one pair of the most important electrochemical reactions. The promising applications are primarily due to their unique physical and chemical properties, such as high surface area, access to large quantities, tunable electronic/ionic conductivity, unique graphitic basal plane structure, and the easiness of modification or functionalization. Chemical doping with heteroatoms (e.g., N, B, P, or S) into graphitic domains can tune the electronic properties, provide more active sites, and enhance the interaction between carbon structures and oxygen molecules. Meanwhile, GO/rGO has demonstrated excellent performances in electric double-layer capacitors (EDLCs, also known as supercapacitors or ultracapacitors) with excellent volumetric and gravimetric capacitance densities as well as feasibility in design and fabrications. Additionally, rGO holds great promise to be high-performance anode materials in lithium-ion batteries due to its favorable interactions with Li. In this chapter, we will discuss the uses of GO/rGO derivatives in these energy conversion and storage technologies, providing insights and guidance for further optimization and design of multifunctional materials for energy applications.

Keywords Graphene oxide • Electrocatalysis • Fuel cells • Supercapacitors • Lithium batteries

G. Wu (✉)
Department of Chemical and Biological Engineering, University at Buffalo, The State University of New York, Buffalo, NY 14260, USA
e-mail: gangwu@buffalo.edu

W. Gao
The Department of Textile Engineering, Chemistry & Science, College of Textiles, North Carolina State University, Raleigh, NC 27695, USA
e-mail: wgao5@ncsu.edu

W. Gao (ed.), *Graphene Oxide*, DOI 10.1007/978-3-319-15500-5_4

4.1 GO/rGO-Derived Nonprecious Metal Catalysts

4.1.1 Overview

Energy conversion and storage via direct electrochemical reactions are one of the most important energy technologies of modern day, including polymer electrolyte fuel cells (PEFCs), metal (Li or Zn)-air batteries, and water electrolyzers. These devices offer many advantages over traditional fossil fuel combustion technologies, including improved overall efficiency, high energy density, and the significant reduction of CO_2 and other emissions. PEFCs are high-efficiency chemical-to-electrical energy conversion devices that can be used as power sources in electric vehicles and portable and stationary applications. Metal–air batteries can provide vastly enhanced energy densities over traditional lithium-ion batteries. For example, compared to other rechargeable systems, Li–O_2 batteries, as a possible next-generation energy storage and conversion device, have attracted much attention due to their very high energy density. Unlike the traditional intercalation electrodes used in Li-ion batteries, the porous cathode in the Li–O_2 cell is capable of taking reactant O_2 from the atmosphere, instead of storing bulky reactants in the electrode. As a result, the battery has significantly improved specific energy density (theoretical value of 5,200 Wh/kg) [1], which has great promise to meet the battery targets set for automotive applications (1,700 Wh/kg, derived from the practical energy density of gasoline) [2, 3]. Additionally, these metal–air batteries can be widely used to store clean energy obtained from renewable wind and solar sources and can also be used for grid-scale energy storage in power plants. Noteworthy, both fuel cells and metal–air cells have similar oxygen cathodes and share the same operating principles for the ORR and OER [4].

Due to the high overpotentials of ORR and OER and inherently slow reaction kinetics, the performance of these electrochemical energy technologies is greatly limited by ORR and OER activities [5–7]. Pt- and Ir-based catalysts represent the state of the art for the ORR and OER, respectively, in terms of their highest activity and durability. To realize a sustainable development, replacing these precious metals with highly active and stable nonprecious metal catalysts (NPMCs) has thereby become a very important topic in the field of electrocatalysis. Importantly, exploring advanced catalyst designs and synthesis strategies using earth-abundant elements (e.g., Fe, Co, N, and C) will be a scientific interest with the potential to provide fundamental knowledge and understanding in the field of chemical catalysis and electrochemical science.

Graphene oxide (GO) is a major precursor for preparing graphene and has attracted substantial attention recently. GO is usually made through oxidation of graphite powder under harsh chemical conditions. The most effective method currently used is Hummers method involving a few strong oxidants (e.g., $KMnO_4$, H_2SO_4, and $K_2S_2O_8$). As a result, different oxygen-containing groups, especially hydroxyl, epoxy, and carboxyl, are formed on both sides and at the edges. Importantly, GO flakes can be exfoliated into single-layer and multilayer sheets

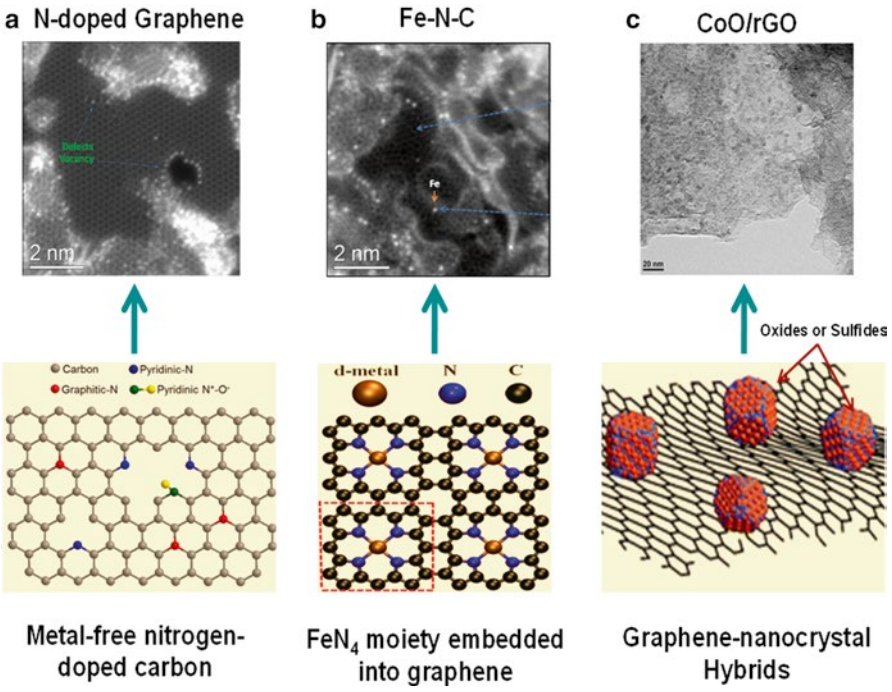

Fig. 4.1 Currently studied graphene-based catalysts: (**a**) metal-free nitrogen-doped graphene. Reprinted with permission from Ref. [9]. Copyright 2012 American Chemical Society (**b**) transition metal incorporated graphene. Reproduced from Ref [8] by permission of the Royal Society of Chemistry. (**c**) Transition metal-compound/graphene hybrid catalysts. Reproduced from Ref [10] by permission of the Royal Society of Chemistry

when dissolved in water due to the strong coulombic repulsion between hydrolyzed sheets. In order to prepare graphene materials, a complete reduction process for GO is needed to remove all of oxygen-containing functionalities from GO surface to prepare electrically conductive reduced GO (rGO).

Generally, the current applications of GO/rGO in ORR catalysts can be divided into three categories (Fig. 4.1) [8–10]. (1) At first, heteroatoms, such as N, can dope into graphitic basal planes and change the electronic and structural properties, providing more active sites and enhancing the interaction between carbon structure and oxygen molecules. Theoretical studies have shown that doped nitrogen atoms can be viewed as *n*-type carbon dopants that disorder carbon lattices and donate electrons to carbon, thus facilitating the ORR activity. (2) Secondly, there is increasing evidence showing transition metal cations, especially Fe, are able to bond with nitrogen and embedded into the basal planes. This configuration was proposed as a possible active site with much improved intrinsic activity, compared to metal-free nitrogen-doped graphene structures. (3) In the third case, transition metal nanocrystals including oxides and sulfides have been found to be catalytically active for ORR or OER. When depositing such nanocrystal onto active sp^2 carbon lattice, a

synergetic effect may rise between the active species in graphene planes and these loaded transition metal nanocrystals, thereby leading to much improved activity.

In our recent effort to develop high-performance NPMCs for ORR, the formation of graphene-like morphology in catalysts is more closely associated with the enhancement of catalyst activity and stability. The graphene-rich TiO_2-supported catalyst has higher activity, compared to the Ketjenblack-supported catalysts [11]. Meanwhile, the graphene-containing MWNTs supported catalysts exhibited much enhanced performance durability, compared to other catalyst without graphene [12]. Thus, the existence of graphene seems to have a promotional role in improving catalyst performance. These results suggest that GO/rGO-based catalysts provide new opportunities on catalyst development for electrochemical energy conversion and storage. In the meantime, from the fundamental research point of view, studying catalytic properties of graphitic domain will be of importance to materials chemistry and engineering research.

Thus, in this chapter, we primarily focus on the recent development of GO/rGO composite electrocatalysts for ORR and their applications in fuel cells and metal–air batteries. Various GO/rGO composite materials including metal-free heteroatom (N and S)-doped rGO, transition metal-derived nitrogen-doped rGO (M–N–C) catalysts, and transition metal-compound/rGO hybrids are discussed in terms of their correlations among synthesis, structures/morphology, ORR activity, and the corresponding alkaline fuel cells or metal–air batteries performance under real working conditions.

4.1.2 Heteroatom-Doped rGO Catalysts

Recently, the research on exploring the use of graphene nanocomposites as metal-free catalysts has been one of the major subjects for the ORR cathode for alkaline fuel cells and metal–air batteries [13]. Due to the low cost, environmental acceptability, corrosion resistance, high electrical conductivity, and good ORR activity in alkaline media, graphene materials are viewed as ideal candidates for metal-free catalyst for these energy storage and conversion technologies. Generally, among different allotropes of carbon, graphene with ordered graphitic structure are expected to facilitate the electron transfer rate and exhibit good electrochemical stability. Importantly, it has been commonly recognized that heteroatom doping into sp^2 carbon lattice leads to much improved ORR activity [14, 15]. In this section, we discuss the synthesis, structures, and applications of such metal-free heteroatom-doped rGO composite catalysts.

4.1.2.1 Nitrogen-Doped rGO Catalysts

While traditional carbon materials (e.g., carbon blacks, nanotube, fibers) are capable of being good catalyst supports, they generally exhibit insufficient catalytic activity for the ORR [16]. Historically, several methods have been used to modify

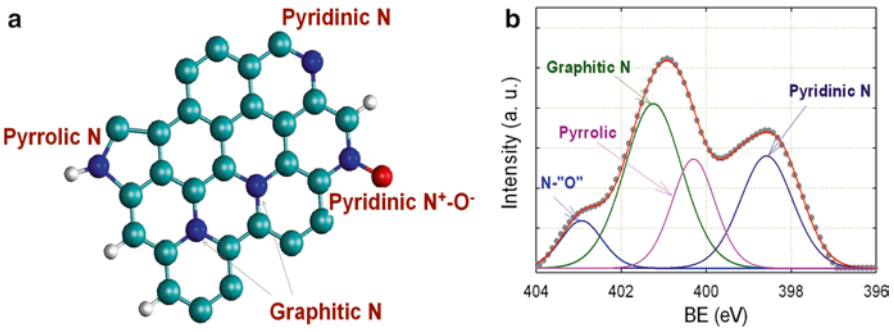

Fig. 4.2 (**a**) Nitrogen doping into carbon plane at different location; (**b**) typical binding energies of nitrogen atoms in different doping environment determined by X-ray photoelectron spectroscopy. Reproduced from Ref [17] by permission of the Royal Society of Chemistry

these carbon materials in an effort to improve their catalytic performance. Apart from optimization of morphological properties (e.g., surface area and porosity), chemical modification of the carbon has been explored to improve intrinsically catalytic activity. Importantly, chemical doping with heteroatoms (e.g., N, B, P, or S) into carbon lattice can tune the electronic and geometric properties, provide more active sites, and enhance the interaction between carbon structure and oxygen molecules. Among various heteroatoms, nitrogen doping plays a critical role in modifying carbon structures due to comparable atomic size of nitrogen and carbon, as well as the presence of five valence electrons in the nitrogen atoms available to form strong covalence bonds with carbon atoms.

As shown in Fig. 4.2 [17], various nitrogen doping into carbon can be identified by different binding energies in X-ray photoelectron spectroscopy (XPS) associated with dominant pyridinic (398.6 ± 0.3 eV) and graphitic nitrogen (401.3 ± 0.3 eV) [18]. Pyridinic nitrogen is obtained by doping at the edge of the graphene layer, contributing one $p\pi$ electron to the graphitic π system. Quaternary nitrogen is the result of in-plane doping and contributes two $p\pi$ electrons. In addition, the pyrrolic form of nitrogen (400.5 ± 0.3 eV) observed at the relatively low heat-treatment temperature (600–700 °C) is assigned to nitrogen atoms in a pentagon structure, which is indistinguishable in XPS from pyridone (pyridinic nitrogen next to an OH group) [19, 20]. Both pyrrolic and pyridone nitrogens have been shown to decompose at temperatures above 800 °C to either pyridinic or quaternary nitrogen [19–22]. Nitrogen species with a high binding energy (402–405 eV) can be assigned to oxidized nitrogen, such as a pyridinic N^+–O^- species [19]. In particular, quaternary and pyridinic nitrogens are dominant nitrogen doping in such nitrogen-doped carbon catalysts and crucial to ORR activity.

In the case of graphitic nitrogen, before the doping, density functional theory (DFT) calculations indicated that the electron density of carbon planes is uniform showing insignificant activity for ORR. However, doping of graphitic N into graphene structure leads to a nonuniform electron distribution, especially when two quaternary N are doped into the same hexagon unit. As a result, the nonuniform

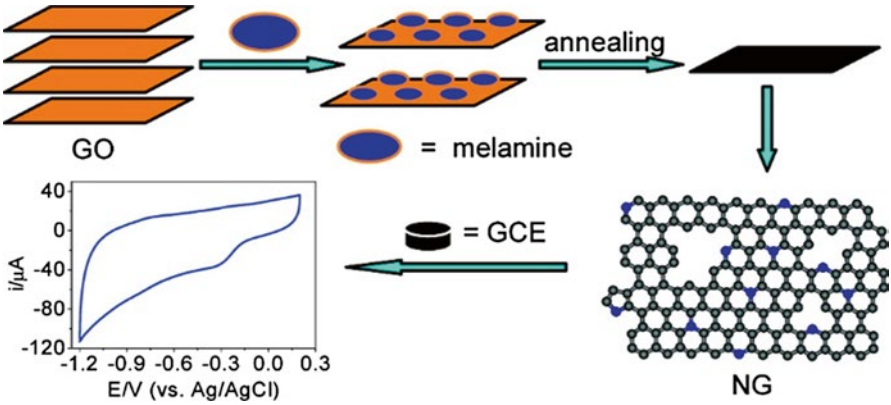

Fig. 4.3 Illustration of the nitrogen doping process of melamine into GO layers [1]. Melamine adsorbed on the surfaces of GO when temperature is <300 °C [2]. Melamine condensed and formed carbon nitride when temperature is <600 °C [3]. Carbon nitride decomposed and doped into graphene layers when temperature is >600 °C. Reprinted with permission from Ref [32]. Copyright (2011) American Chemical Society

electron density which resulted from graphitic N doping will enhance catalytic activity of carbon. In the meantime, from the geometric point of view [23], doping of graphitic nitrogen in plane will make the C–N bonds much shorter and is comparable to O–O bonds. This change will facilitate O_2 adsorption and subsequent disassociation of O–O bonds. The pyridinic N sites have been widely received as catalytic active sites for ORR, because XPS experiments showed that the highly catalytic carbon materials usually have a large amount of pyridinic nitrogen. Using graphene nano-ribbon models, the DFT calculation also indicated the pyridinic N doped at the edge can reduce the energy barrier for oxygen adsorption on adjacent carbon atoms. In addition, doping of N at the edge of graphene can accelerate the rate-limiting first-electron transfer during the ORR [24].

Currently, nitrogen functionalization of rGO can be realized by several methods, such as heat annealing with NH_3 [25, 26], arc discharge [27, 28], nitrogen plasma [29, 30], and hydrothermal reaction with NH_4OH [31]. As a result, a great number of N-doped rGO electrocatalysts have been developed toward the ORR. Recently, a facile, catalyst-free thermal annealing approach was proposed for large-scale synthesis of N-doped rGO using low-cost industrial material melamine as the nitrogen source (Fig. 4.3) [32]. Typically, GO powder and melamine were ground together in a mortar using pestle for about 5 min, and the mixture was heat-treated at designed reaction temperatures (e.g., 800 °C) for 1 h at a flow of argon [32]. This approach can completely avoid the contamination of transition metal catalysts, and thus, the intrinsic catalytic performance of metal-free N-doped graphene can be investigated. The atomic percentage of nitrogen in the doped graphene samples can be tuned up to 10.1 at.%. It was found that dominant nitrogen atoms are in the form of pyridine, doped at the edge of carbon planes. The resulting N–rGO exhibited excellent electrocatalytic activity for the ORR in alkaline electrolytes, similar to what was

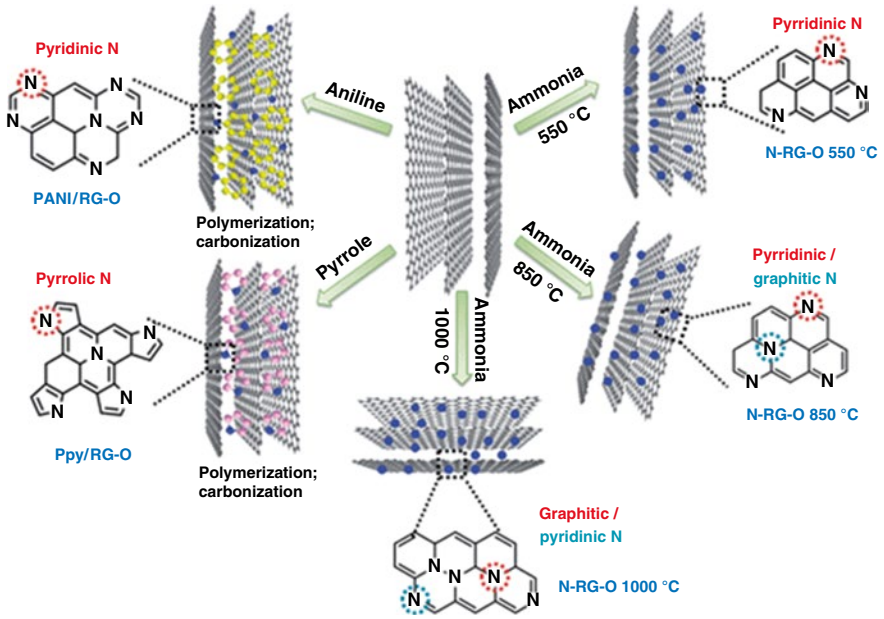

Fig. 4.4 Schematic diagram for the preparation of N-doped graphene with different N states. N–rGO 550, 850, and 1,000 °C are prepared by annealing of GO powder at temperatures of 550, 850, and 1,000 °C under a NH_3·N precursor. PANi/rGO and PPy/rGO are prepared by annealing of PANII/GO and PPy/GO composites at 850 °C. Reproduced from Ref [33] by permission of the Royal Society of Chemistry

observed in nitrogen-doped vertically aligned carbon nanotubes prepared by CVD or other methods [14, 15]. Importantly, the measured electrocatalytic activity with the N–rGO is not greatly dependent on nitrogen content in rGO. It may suggest that, besides of nitrogen doping, morphology and structure of rGO is also important for the electrocatalytic activity toward the ORR.

In order to understand the relationship between the type and concentration of N species and their corresponding catalytic activity, a series of N-doped rGO catalysts were prepared by annealing GO under ammonia or different N-containing polymers (e.g., polyaniline—PANI, polypyrrole—PPy) [33], as demonstrated in Fig. 4.4. The observed superior ORR catalytic activity of N–rGO catalysts prepared by annealing of GO with various N-containing polymer composites is directly linked to both pyridinic N and graphitic N. Annealing of PANI/rGO and PPy/rGO leads to predominate pyridinic N and pyrrolic N species, respectively. Most importantly, the electrocatalytic activity of N-containing metal-free catalysts is highly dependent on the graphitic N content while pyridinic N species improve the onset potential for ORR. In good agreement with others, the total atomic content of N in the metal-free, graphene-based catalyst did not play an important role in the ORR process. Graphitic N can greatly increase the limiting current density, while pyridinic N species might convert the ORR reaction mechanism from a $2e^-$-dominated process to a $4e^-$-dominated process [33].

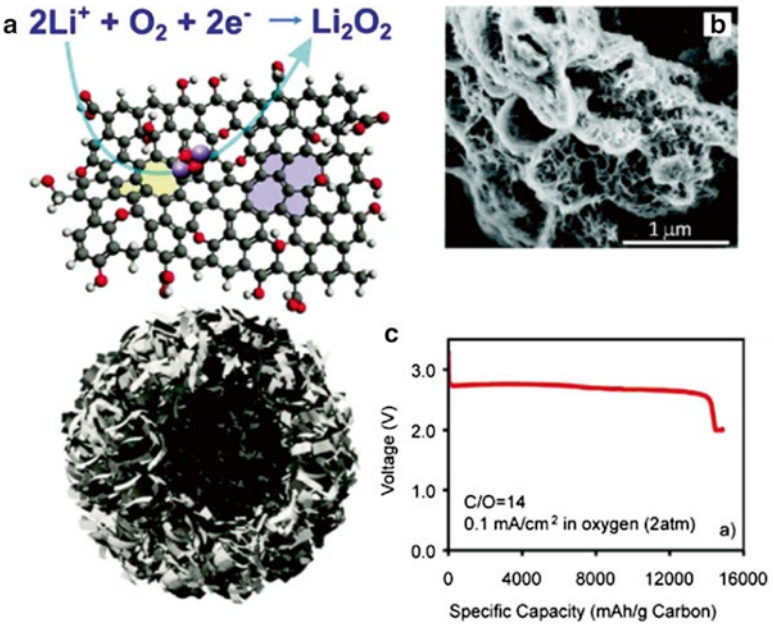

Fig. 4.5 (**a**) Schematic structure of a functionalized graphene sheet (*upper image*) with an ideal bimodal porous structure (*lower image*) which is highly desirable for Li–O_2 battery operation. (**b**) SEM images of as-prepared rGO (C/O = 14). (**c**) The discharge curve of a Li–O_2 cell using rGO(C/O = 14) as the air electrode (P_{O2} = 2 atm). Reprinted with permission from Ref. [35]. Copyright (2011) American Chemical Society

rGO also has become one of the most promising catalysts for the ORR in nonaqueous electrolyte for Li–O_2 batteries. Recently, rGO nanosheets (GNSs) have been successfully established in an air electrode for nonaqueous batteries [31, 34]. The air electrode based on rGO GNSs yielded a high discharge capacity of ~8,700 mAh g^{-1} at a current density of 75 mA g^{-1}, compared to ~1,900 mAh g^{-1} for BP-2000 and ~1,050 mAh g^{-1} for Vulcan XC-72, respectively. The dominant discharge product was Li_2CO_3 and a small amount of Li_2O_2. This result indicated that rGO can be used as an advanced cathode catalyst for Li–air batteries. Recently, Xiao and coworkers used a colloidal microemulsion approach and demonstrated the construction of hierarchically porous air electrodes with functionalized rGO sheets that contain lattice defects and hydroxyl, epoxy, and carboxyl groups. Figure 4.5a shows the schematic structure of functionalized graphene with an ideal bimodal porous structure which is highly desirable for Li–O_2 battery operation. Unlike conventional two-dimensional (2D) layered graphene sheets that hinder the rapid gas diffusion that is essential for the efficient operation of Li–air batteries, the three-dimensional (3D) air electrodes developed in this work via the thermal expansion and simultaneous reduction of GO consisting of interconnected pore channels on both the micro- and nanometer length scales (Fig. 4.5b) are ideally suited for air electrodes since the pores on different length scales may facilitate oxygen diffusion,

avoiding pore blockage due to Li_2O_2 deposition during discharge in nonaqueous Li–O_2 batteries. DFT calculation and electron microscopy characterization suggest that the functional groups and lattice defects play a critical role in improving the battery performance by forming small particle size of discharge products. In particular, the C/O = 14 graphene electrode, containing more functional groups, resulting in better performance and smaller Li_2O_2 particles, when compared to those of C/O = 100 with less functional groups. Importantly, in the unique hierarchical structures, large tunnels constructed by the macropores facilitate oxygen transfer into the air electrode, and small "pores" are able to provide ideal multiphase regions for the ORR. Thus, the combination of the abundance of functional groups and the hierarchical pore structures leads to an exceptionally high capacity of 15,000 mAh g^{-1} during the discharge process (Fig. 4.5c).

4.1.2.2 Other Heteroatom-Doped rGO Catalysts

In addition to nitrogen doping into carbon materials, other elements such as boron, phosphorous, and sulfur are also able to dope into carbon lattice, modifying geometric and electronic structures of graphitic planes and affecting the catalytic activity toward the ORR.

Sulfur (electronegativity of sulfur: 2.58) has a close electronegativity to carbon (electronegativity of carbon: 2.55). S doping into sp^2 carbon lattice may play the similar role to nitrogen in enhancing catalytic activity. It was found by Bandosz and coworkers that rGO in confined space of silica gel nanopores doped with sulfur shows high catalytic activity for the ORR in alkaline medium and exhibits a superior tolerance to the presence of methanol [36]. In particular, the treatment with hydrogen sulfide at 800 °C of rGO resulted in an incorporation of 2.8 at.% sulfur in the rGO layers. XPS analysis indicated that this sulfur is mainly in the form of elemental sulfur/polysulfides (0.18 at.%), R–SH groups (2.28 at.%), C–S–C/R–S_2–OR configuration (0.21 at.%), and R_2–S = O (0.13 at.%) functionalities. The good performance of the S-doped material is linked to the coexistence of sulfur and oxygen on the surface in equal atomic quantities and a unique porosity being the replica of the silica pores. The former leads to the positive charge on the carbon atoms, which are the reaction sites. Importantly, enhanced hydrophobicity of the surface and the resulting meso/micropores could further enhance the adsorption of O_2. In addition, N and S dual-doped mesoporous graphene has also been reported as a metal-free catalyst for ORR in alkaline medium [37]. The DFT calculations have revealed that the introduction of sulfur to the carbon matrix can be associated with the mismatch of the outermost orbitals of sulfur and carbon due to their close electronegativity. Thus, the S atom is positively charged and hence can be viewed as the catalytic center for ORR. The synergistic performance enhancement is due to the redistribution of spin and charge densities resulting from the dual doping of S and N atoms, which leads to a large number of active carbon atom sites.

In addition, Yang et al., demonstrated a successful preparation of sulfur-doped graphene (S-graphene) by directly annealing GO and benzyl disulfide (BDS) in

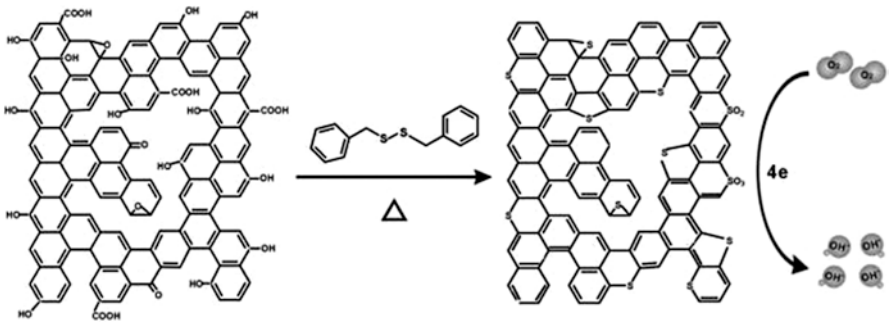

Fig. 4.6 Schematic illustration of S-graphene preparation. Reprinted with permission from Ref. [38]. Copyright (2011) American Chemical Society

argon (Fig. 4.6) [38]. Typically, the experimental scheme for S-graphene preparation is illustrated in a typical procedure—GO and BDS were first ultrasonically dispersed in ethanol. The resulting suspension was spread onto an evaporating dish and dried at 40 °C, forming a uniform solid mixture. The mixture was placed in a quartz tube under an argon atmosphere and annealed at 600–1,050 °C. The final products were collected from the quartz tube. The contents and bonding configurations of sulfur in these S-graphenes can be adjusted by varying the mass ratios of GO and BDS or the annealing temperature. The prepared graphene sheets are wrinkled and folded. The S distribution in the plane of S-doped graphene is relatively uniform. The electrocatalytic activity shows that the S-graphene can exhibit excellent catalytic activity, long-term stability, and high methanol tolerance in alkaline media for ORRs. Moreover, we find also that the graphene doped with another element which has a similar electronegativity as carbon such as selenium (electronegativity of selenium: 2.55) shows a similarly high ORR catalytic activity. The experimental results are believed to be significant because they not only give further insight into the ORR mechanism of these metal-free doped carbon materials but also open a way to fabricate other new low-cost NPMCs with high electrocatalytic activity by a simple, economical, and scalable approach for fuel cell applications.

DFT calculations revealed that electron-deficient boron dopants were positively charged in the B-doped carbon lattice and induced the chemisorptions of oxygen molecules on doped carbon. The electrocatalytic activity derived from B doping for the ORR is derived from the electron accumulation in the vacant 2*pz* orbital of boron dopant from the π^* electrons of the conjugated system, which then transfers to the chemisorbed oxygen molecules through boron as a bridge. The transferred charge is able to weaken the O–O bonds and thus facilitate the ORR [39].

Recently, Xia et al. [40] reported a facile, effective, and catalyst-free thermal annealing approach to preparing boron-doped graphene (Fig. 4.7) on a large scale using boron oxide as the boron source. Boron-doped graphene was synthesized through thermal annealing GO, synthesized by the modified Hummers method in the presence of boron oxide (B_2O_3), where boron atoms coming from B_2O_3 vapor can replace carbon atoms within graphene structures at high temperature in a homemade tubular furnace. In a typical procedure, GO powder was put onto the surface of B_2O_3

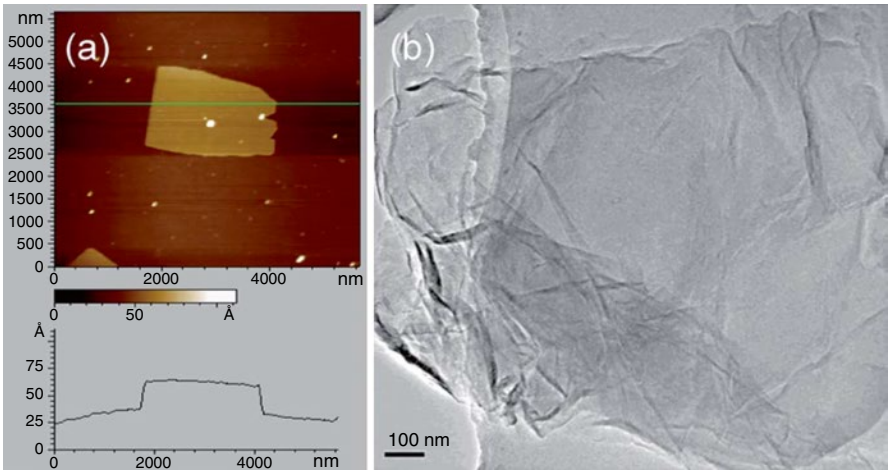

Fig. 4.7 Typical AFM image (**a**) and low-resolution TEM image (**b**) of BG. Reproduced from Ref [40] by permission of the Royal Society of Chemistry

in a corundum crucible, which was then placed in the center of a corundum tube with a continuous flow of argon to guarantee an inert atmosphere in the tube furnace. The center temperature of the furnace was heated to 1,200 °C at an increasing rate of 5 °C min^{-1}. After maintaining at this temperature for 4 h, the sample was cooled to room temperature slowly under an Ar atmosphere. The obtained product was then refluxed in 3 M NaOH aqueous solution for 2 h to remove any of the unreacted boron oxide. After filtration and water washing, the product was dried in a vacuum at 60 °C. For comparison, pristine graphene was also prepared using a similar procedure but without adding B_2O_3. Compared to pristine graphene, the product BG exhibits excellent electrocatalytic activity and long-term stability toward ORR in alkaline electrolytes and good tolerance to poisons. Although the functioning mechanism of doped boron in graphene is not clear yet, this will not prevent us using it as a promising metal-free catalyst toward ORR in fuel cells and other catalytic applications.

In summary, above are discussion of heteroatom-doped metal-free rGO catalysts in terms of their synthesis, structures/morphologies, and the resulting catalytic activity for the ORR in various electrolytes for electrochemical energy storage and conversion. It is scientifically important to explore the enhancement of catalytic activity of rGO by modifying its electronic and geometric structure through chemical dopants. It is worth noting that the currently studied metal-free rGO catalysts are capable of efficiently catalyzing the ORR in alkaline media, even exceeding the Pt catalysts. However, these metal-free rGO catalysts always suffer the low activity and high peroxide yield during the ORR in acidic electrolyte. The variance of ORR activity in both alkaline and acidic media suggests that, among different possible active sites (CN*x*, MN*x* or MCN*x*, M = Co or Fe), the most active site structures for the ORR in alkaline and acidic electrolytes are likely not the same, due to their different reaction mechanisms. Especially, the abundant CN_x structures in alkaline media may be active enough to catalyze ORR, but still insufficient in acidic media.

4.1.3 Transition Metal-Doped rGO Catalysts

As we discussed above, although the metal-free rGO catalysts exhibited good catalytic activity in alkaline media, they are currently suffering poor activity in more challenging acid electrolyte that is very important for Nafion®-based polymer electrolyte fuel cells. However, it was found that the incorporation of transition metals especially Fe can lead to significant enhancement of the ORR activity of rGO in acidic electrolyte. Yang Shao-Horn' group first reported such type of Fe-based rGO catalysts [41]. As shown in Fig. 4.8, the synthesis procedure can be divided into three steps. At first, g-C_3N_4 and $FeCl_3$ (6 wt%) were well mixed in water. Then GO was added to the suspension followed by a reduction using a mixed NH_3/N_2H_4 solution at 80–100 °C. Secondly, the resulting powder mixture ($FeCl_3$/g-C_3N_4/rGO) was collected after drying via vacuum filtration. Noteworthy, the g-C_3N_4 precursor was polymerized thermally from dicyandiamide and employed as the nitrogen source. The resulting $FeCl_3$/g-C_3N_4/rGO mixture showed a homogeneous dark green color that was derived from the yellowish $FeCl_3$ and g-C_3N_4 and the black rGO.

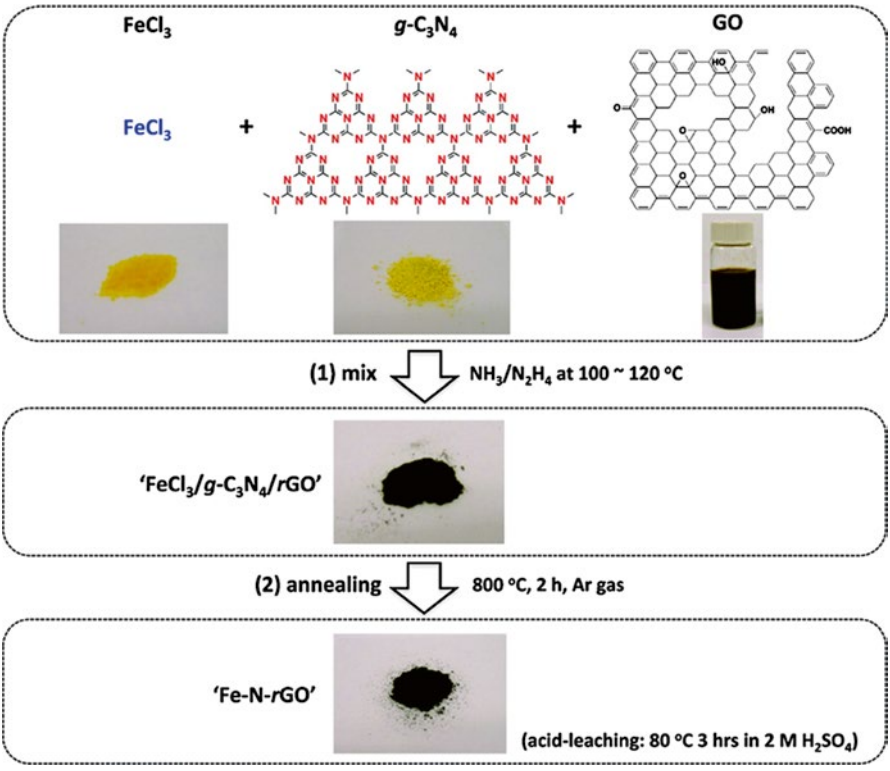

Fig. 4.8 Schematic illustration of Fe–N–rGO synthesis and optical images of powder samples at various stages of synthesis. Reprinted with permission from Ref. [41]. Copyright (2013) American Chemical Society

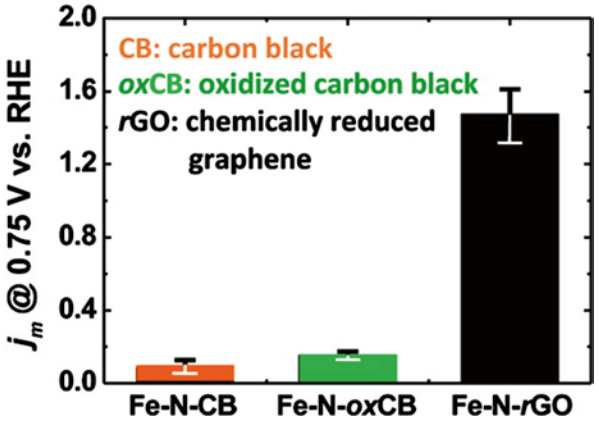

Fig. 4.9 Comparison of ORR mass activity from RDE measurements in O_2-saturated 0.5 M H_2SO_4 at 10 mV s^{-1} of scan rate and 900 rpm of rotation rate. Reprinted with permission from Ref. [41]. Copyright (2013) American Chemical Society

In the third step, the mixture was heat-treated at 800 °C for 2 h under Ar atmosphere. During the high temperature treatment, significant mass loss was observed, especially at 200–300 °C for the removal of residual oxygen-containing groups on rGO. Additionally, the second mass loss of ~65 wt% occurs in the temperature range from 620 to 700 °C due to sublimation of g-C_3N_4.

As shown in Fig. 4.9, the ORR mass activity of the Fe–N–rGO was determined at 0.75 V vs. RHE, yielding a current density of ~1.5 mA mg^{-1}. This value is seven times higher compared to other carbon black or oxidized carbon black supported Fe–N–C catalysts. The stability of Fe–N–rGO for ORR was further evaluated at a constant potential at 0.5 V in O_2-bubbled 0.5 M H_2SO_4 at 80 °C. Fe–N–rGO was found to have higher stability than other traditional carbon black supported Fe–N–C catalysts. It is hypothesized that the enhanced stability of Fe–N–rGO for ORR is due to enhanced degree of graphitization of Fe–N–rGO. In addition, significantly reduced H_2O_2 during the ORR observed with the Fe–N–rGO catalysts is beneficial for improving the stability. Thus, the rGO-based Fe catalyst exhibited much enhanced ORR mass activity and stability approaching those of the state-of-the-art non-noble-metal catalysts reported to date. This effort demonstrated that utilizing the unique surface chemistry of rGO is able to create active Fe–N_x sites and develop highly active and stable catalysts for the ORR in PEFC.

4.1.4 rGO/Oxide Hybrids Catalysts

Metal oxides, especially manganese and cobalt oxides, are found for a long time to be active for oxygen reaction in alkaline solution [42, 43]. However, inherent low conductivity is one of the important drawbacks that limit their application as ORR

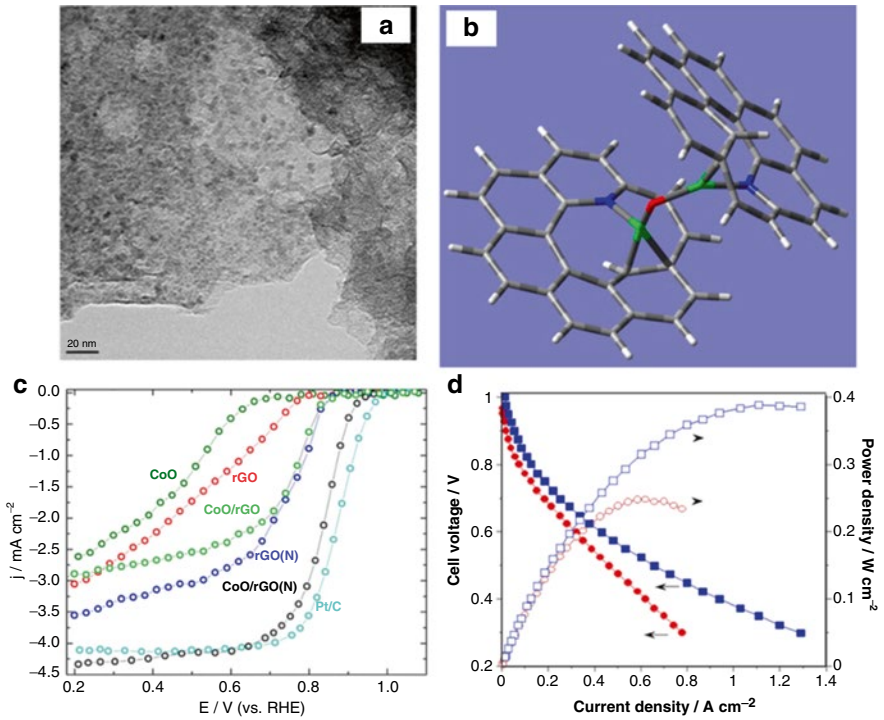

Fig. 4.10 (**a**) CoO/rGO(N) catalyst morphology. (**b**) Optimized rGO(N)–Co(II)–O–Co(II)–rGO(N) using highest occupied molecular orbital (HOMO) at the B3LYP/6-31G level of theory. Carbon (*gray*), nitrogen (*blue*), cobalt (*green*), and oxygen (*red*). (**c**) Steady-state RDE polarization plots for ORR on CoO/rGO(N) catalyst and other controls (CoO, rGO, rGO(N), Pt/C) in 0.1 M O_2-saturated KOH at 25 °C and 900 rpm. (**d**) Anion-exchange-membrane H_2 (at 1 atm, 57 % RH)/O_2 (at 1 atm, 100 % RH) fuel cell tests using Pt/C (*square symbol*) and CoO/rGO(N) cathodes (*circle symbol*) at 60 °C. Reprinted with permission from Ref. [48]. Copyright (2013) American Chemical Society

cathodes in alkaline fuel cell. In order to overcome this challenge, these simple metal oxides need to be combined with other highly electrically conductive materials for preparing composite ORR electrocatalysts. Recently, a class of nanocarbon/transition metal oxides or sulfides hybrid catalysts for ORR in alkaline media were extensively studied in Dai's group at Stanford University by rGO, which includes Co_3O_4/N–rGO [31], $MnCo_2O_4$/N–rGO [42], $Co_{1-x}S$/rGO [44], etc. Besides manganese- or cobalt-based catalysts, a large variety of metal oxides have also been studied as ORR catalyst in alkaline solution, including Cu_2O/rGO [45, 46] and Fe_3O_4/N–rGO aerogel [47].

Recently, we reported a novel graphene composite CoO/rGO(N) catalyst containing high loading cobalt oxide (24.7 wt%, Co) via depositing CoO nanoparticles onto nitrogen-doped rGO (rGO(N)), as shown in (Fig. 4.10a) [48]. The Co(II) is identified as a dominant cobalt species on catalysts and most likely coordinately coupled with pyridinic N doped into graphene planes, evidenced by X-ray absorption spectra and DFT calculations (Fig. 4.10b). In particular, DFT calculations suggest that CoO

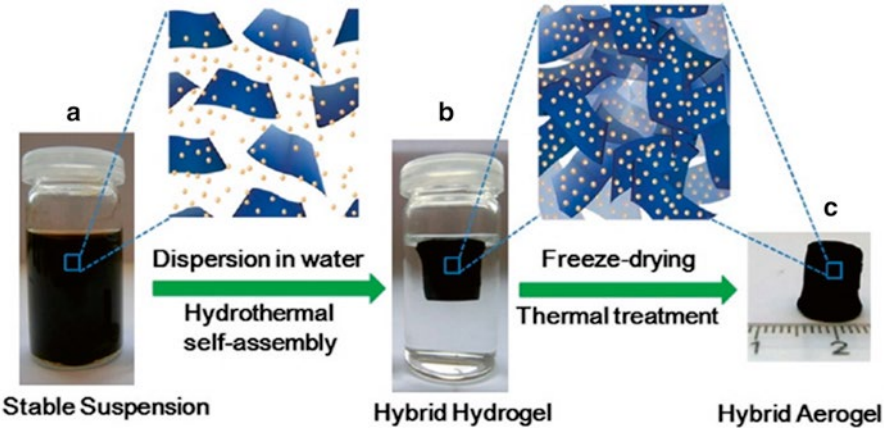

Fig. 4.11 Fabrication process for the 3D Fe_3O_4/N–rGO catalyst. (**a**) Stable suspension of GO, iron ions, and PPy dispersed in a vial. (**b**) Fe- and PPy-supporting graphene hybrid hydrogel prepared by hydrothermal self-assembly and floating on water in a vial and its ideal assembled model. (**c**) Monolithic Fe_3O_4/N–rGO hybrid aerogel obtained after freeze-drying and thermal treatment. Reprinted with permission from Ref. [47]. Copyright (2012) American Chemical Society

can strongly couple with pyridinic nitrogens in the rGO(N) and thus form a stable structure represented as rGO(N)–Co(II)–O–Co(II)–rGO(N). With this unique structure, a synergistic effect between rGO(N) and cobalt oxide may facilitate the ORR in alkaline media, yielding a much improved activity ($E_{1/2}$ ~0.83 V vs. RHE) and four electron selectivity, when compared to either rGO(N) or CoO along (Fig. 4.10c). The developed catalysts were also tested in anion-exchange-membrane alkaline fuel cells using the AS4 anion exchange ionomer (Tokuyama). Importantly, due to the richness of defects and nitrogen doping, the graphene-based supports can accommodate a high Co loading, leading to a thin cathode layer with enhanced mass transfer in alkaline fuel cell cathode. As a result, the thickness of the catalyst layer of the MEAs is less than 20 nm, which is close to the MEA prepared with Pt/C catalysts. Compared to the Pt/C cathode, the cell with the CoO/rGO(N) cathode only has a slightly decreased OCV around 38 mV (Fig. 4.10d). A similar downward voltage shift at the low current density range was observed for the CoO/rGO(N) and Pt/C cathodes. At typical operating voltage of ~0.6 V, the power outcome of the CoO/rGO(N) catalyst is approaching that of the Pt/C catalyst.

Three-dimensional (3D) N-doped rGO aerogel-supported Fe_3O_4 nanoparticles (Fe_3O_4/N–rGO) as efficient cathode catalysts for the oxygen reduction reaction (ORR) are reported (Fig. 4.11) [47]. As displayed in Fig. 4.12 [47], the Fe_3O_4/N–rGO hybrids exhibit an interconnected macroporous framework of graphene sheets with uniform dispersion of Fe_3O_4 nanoparticles. XRD patter versifies the formation of Fe_3O_4 during the synthesis. SEM image indicates a significant portion of the nanoparticles which are encapsulated within the graphene layers, suggesting efficient assembly between the Fe_3O_4 and the rGO sheets. In studying the effects of the carbon support on the Fe_3O_4 for the ORR, Fe_3O_4/N–GAs show a more positive onset potential, higher oxygen reduction density, lower H_2O_2 yield, and higher electron transfer number in alkaline

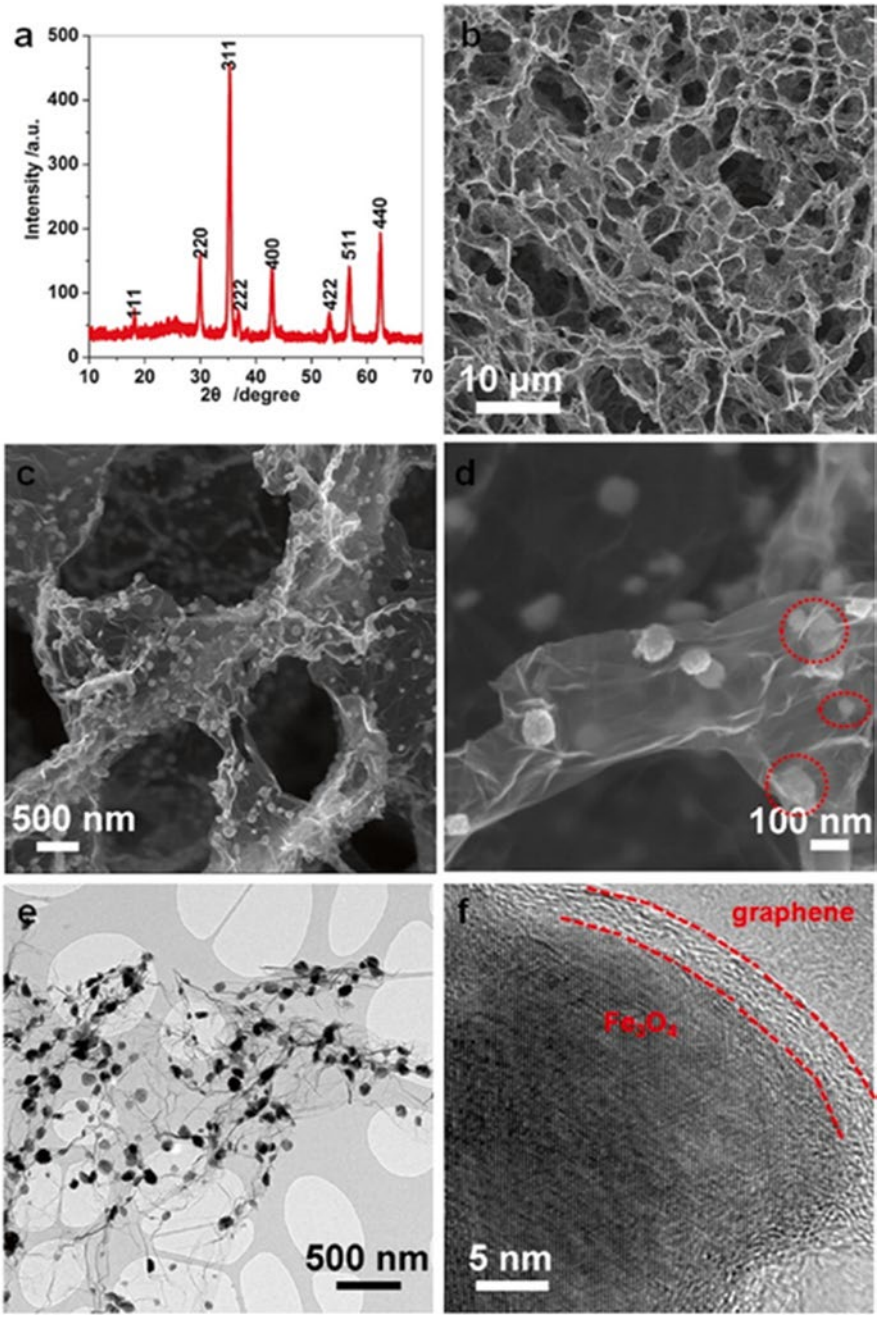

Fig. 4.12 Structure and morphology of Fe_3O_4/N–rGO catalysts. (**a**) XRD pattern and (**b**–**d**) typical SEM images of Fe_3O_4/N–rGOs revealing the 3D macroporous structure and uniform distribution of Fe_3O_4 NPs in the GAs. The red rings in (**d**) indicate Fe_3O_4 NPs encapsulated in thin graphene layers. Representative (**e**) TEM and (**f**) HRTEM images of Fe_3O_4/N–rGO revealing an Fe_3O_4 nanoparticles rapped by graphene layers. Reprinted with permission from Ref. [47]. Copyright (2012) American Chemical Society

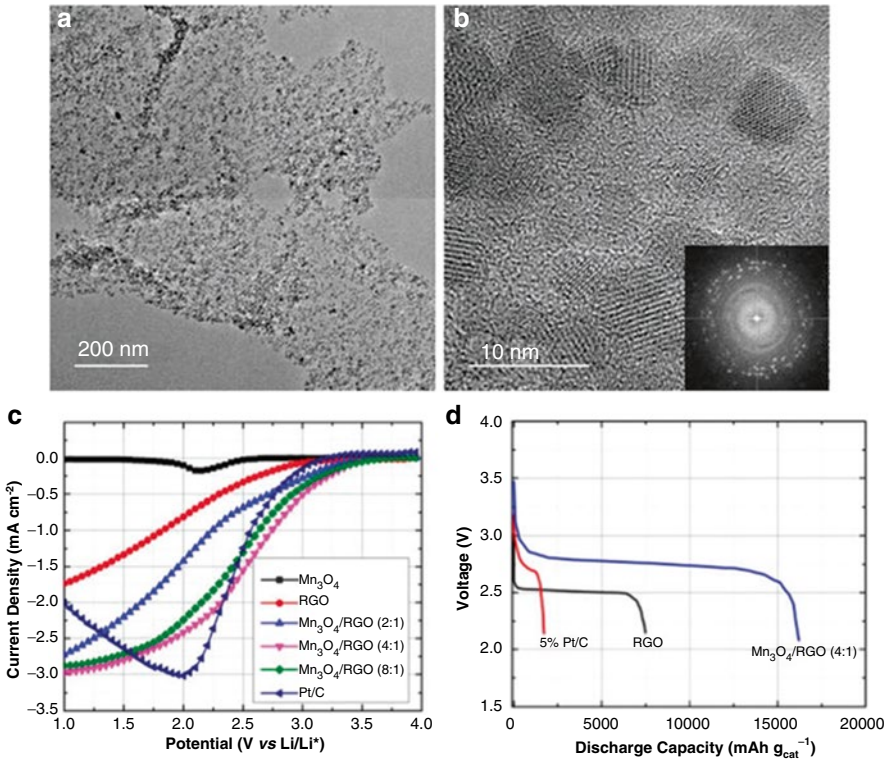

Fig. 4.13 (**a**, **b**) SEM and TEM images of the as-prepared Mn_3O_4/rGO nanocomposites with an rGO to Mn_3O_4 mass ratio of 4:1. (**c**) ORR steady-state RDE polarization curves for various catalysts in O_2-saturated 0.1 M $LiPF_6$ in the DME electrolyte. Rotating speed: 900 rpm; room temperature; (**d**) initial discharge performance of various catalysts at a current density of 50 mAg^{-1} in Li–O_2 battery tests. Reprinted from Ref. [56] by permission of the Royal Society of Chemistry

media, when compared to Fe_3O_4 nanoparticles supported on N-doped carbon black or N-doped rGO sheets. This attests the importance of the 3D macropores and high specific surface area of the GA support for improving the ORR performance. Importantly, better durability was observed with the Fe_3O_4/N–rGO, relative to the commercial Pt/C catalyst. This synthetic effect can be further extended to develop other 3D metal or metal oxide/rGO-based monolithic materials for various applications, such as sensors, batteries, and supercapacitors [47].

Apart from the potential application in aqueous for fuel cell application, such rGO/oxide hybrid catalysts also have attracted increasing interests for the applications in nonaqueous Li–O_2 batteries [49–58]. Recently, we developed a method for one-step synthesis of Mn_3O_4/rGO nanocomposites for nonaqueous Li–O_2 batteries [56]. After 24 h of solvothermal reaction, monodispersed Mn_3O_4 nanoparticles were formed and uniformly bonded on the surface of rGO (Fig. 4.13a). The Mn_3O_4 nanoparticles with diameters of ca. Four to six nanometers are well crystallized (Fig. 4.13b).

Because the monodispersed Mn_3O_4 nanoparticles in our composite have smaller particle size compared to previously reported MnO_x-based composite, it may have a stronger interaction bonding between MnO_x and rGO and lead to higher catalytic activity accordingly [59]. To investigate the cathode catalyst performance, the composite was evaluated by steady-state RDE and Li–O_2 battery test with 1.0 M $LiPF_6$ TEGDME electrolyte (Fig. 4.13c, d). Compared to other ratios of Mn_3O_4 and rGO, the Mn_3O_4/rGO (4:1) catalyst exhibited highest ORR activity in both half-cell and full-cell test, exhibiting an initial discharge capacity as high as 16 000 mAh g^{-1}.

As a new class of ORR catalyst, rGO/transition metal-compound hybrids have attracted more and more attention. However, to date, most of these catalysts still offer inferior performance to that of the Fe–N–rGO catalysts as discussed above. It is partially due to their insufficient inherent activity of oxides or sulfide and low electrical conductivity. Thus, further optimization of the interaction between metal compounds and rGO can further enhance catalyst activity. Noteworthy, these rGO/metal oxide/sulfide catalysts hold great promise to be efficient ORR/OER bifunctional cathode, due to their well-known high OER activity and stability.

4.2 GO/rGOs in Supercapacitors

In addition to their versatile applications in catalysis, GO/rGOs also demonstrated extraordinary promises for energy storage devices such as EDLCs (also known as supercapacitors or ultracapacitors) in the last decade [60–65]. Supercapacitors are relatively new energy storage devices as compared to batteries, conventional electrostatic capacitors, and electrolytic capacitors, adopting unique working principle different from any of the above. As shown in Fig. 4.14, in typical electrostatic

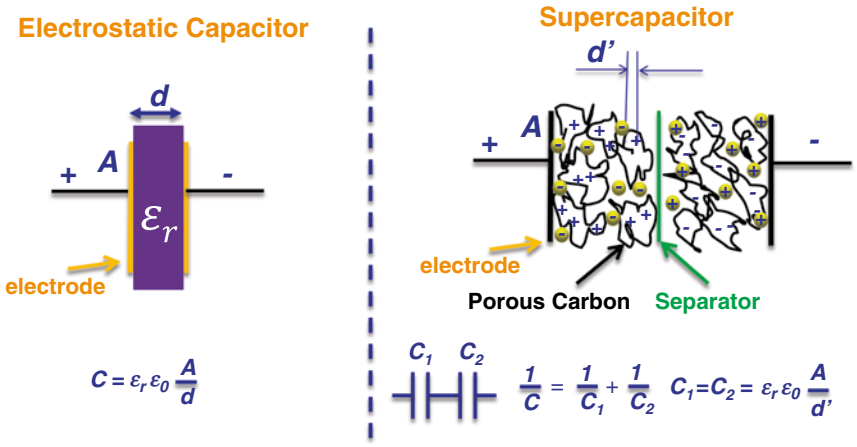

Fig. 4.14 Comparison of different working mechanisms between supercapacitors and conventional electrostatic capacitors

capacitors, two metal plates are separated by a dielectric. The resulted capacitance can be defined as

$$C = \varepsilon_r \varepsilon_0 \frac{A}{d} \tag{4.1}$$

where C represents capacitance, εr represents relative static permittivity, ε_0 represents electric constant (8.854×10^{-12} F/m), A represents the overlapping area of the two plates, and d represents the separation between two plates. However, in the case of supercapacitors, porous carbon materials, such as activated carbons, are used as electrodes, and a macroporous polymer membrane, such as cellulose membranes, is used as the separator. Electrolytes are subsequently added into supercapacitors, in order to form "electric double layers" on porous carbon surfaces. Orders of magnitude higher capacitance is thus generated within the "double layers," which can again be defined by Eq. (4.1). Herein, A becomes the active surface area of porous carbon electrodes ranging from 500 to 3,000 m^2/g. d refers to the separation within the "electric double layers" reported to be between 0.5 and 0.8 nm [66]. A real supercapacitor thus can be viewed as a series connection of two "electric double-layer" capacitors. Thanks to the huge A and minimum d in this structure, commercialized supercapacitors usually have capacitance much higher than their electrostatic counter parts. For example, *Maxwell Technologies* have ultracapacitor cells with capacitance as high as 3,400 F ready for sale. Therefore, EDLCs are important complimentary to batteries in existing energy storage technologies, with superior power density, excellent cycling (>10,000 cycles), but inferior energy density as compared to lithium-ion batteries.

We note that, besides the "electric double-layer capacitance" mentioned here, some supercapacitors also adopt another capacitance mechanism, so-called pseudocapacitance or redox capacitance, which originates from redox reactions of electrochemically active species in electrodes. For example, redox reactions of transition metal cations, such as Mn, Co, or Ru, as well as some surface oxidation of carbons, have been well investigated in this category [67]. Since redox capacitances actually involve faradic processes, they are similar to the electrochemical processes in batteries.

Since 2008, *Ruoff*'s group at University of Texas, Austin, first introduced rGO as active electrodes in supercapacitors [60]. Hydrazine-reduced GO possesses large surface area (theoretical value of 2,630 m^2/g) and good electrical conductivity, which are two key features for an effective electrode material in supercapacitors. The authors reported specific capacitances of 135 and 99 F/g in aqueous and organic electrolytes, respectively (Fig. 4.15) [60]. Three years later, the same research group optimized their recipe of modifications of rGO and obtained a carbon material with surface area as high as 3,100 m^2/g (higher than the theoretical value) and electrical conductivity around 500 S/m. The as-made supercapacitor with the high-surface-area rGO achieved an energy density comparable to lead-acid batteries and a power density an order of magnitude higher than that of the commercial carbon-based supercapacitors [61]. We note that the authors were able to obtain an activated material with effective surface area exceeding the theoretical limit of that of graphene. The major explanation for this is that, with KOH etching treatment, large amounts of

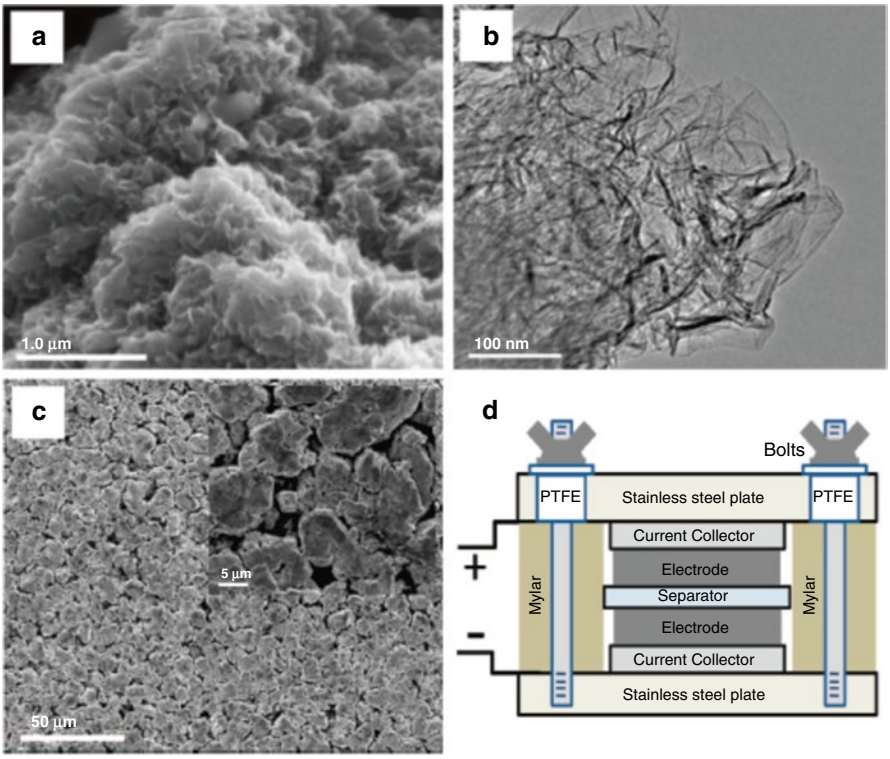

Fig. 4.15 (**a**) SEM image of CMG particle surface, (**b**) TEM image showing individual graphene sheets extending from CMG particle surface, (**c**) low- and high (*inset*)-magnification SEM images of CMG particle electrode surface, and (**d**) schematic of test cell assembly (Reprinted with permission from Ref [60]. Copyright (2008) American Chemical Society)

pinholes were generated on the graphene basal planes, thus significantly increasing the number of active sites for electric double-layer capacitance in the devices.

Later, laser-induced reduction of GO has been heavily exploited by few research groups, leading to fabrication of rGO-based EDLCs with desired geometries and sizes [62–64]. CO_2 laser-patterning technique is widely used in materials engineering for cutting large pieces of plastics or metals. In 2011, Gao et al. first demonstrated the patterning of a freestanding GO film with a CO_2 laser cutter (X660, Universal Laser Systems). The as-made patterns on GO worked instantly as supercapacitors in humid environment (Fig. 4.16) [62]. It is important to note that in this work, the authors also discovered the proton-conducting behavior of hydrated GO films, which was later explored as a proton-exchange membrane in polymer electrolyte fuel cells [68].

Soon after, Kaner's group in University of California at Los Angeles demonstrated similar fabrication processes of EDLCs with a LightScribe DVD optical drive as the reduction tool for GO in 2012 [63, 64]. They coated a thin layer of GO onto a DVD disk and light-scribed it in a computerized DVD drive. The resulted film was peeled

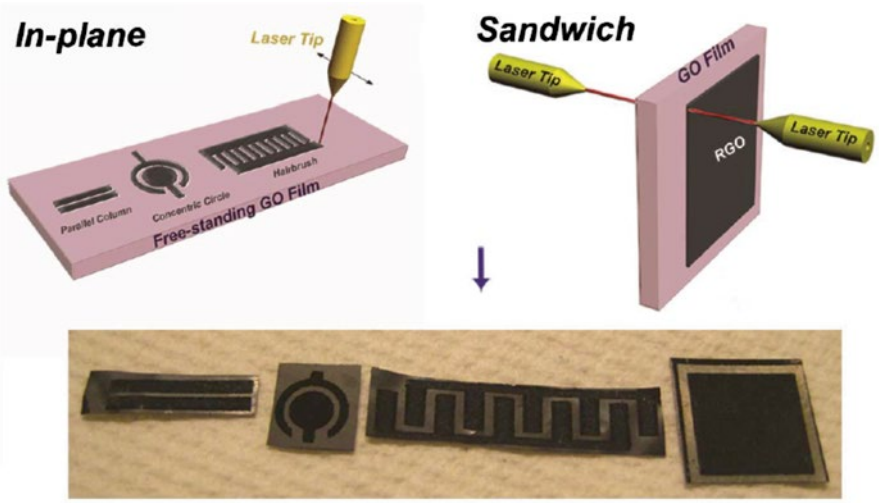

Fig. 4.16 Schematics of CO_2 laser patterning of freestanding hydrated GO films to fabricate RGO–GO–RGO devices with in-plane and sandwich geometries. The *black contrast* in the *top schematics* corresponds to RGO and the light contrast to unmodified hydrated GO. For in-plane devices, three different geometries were used, and the concentric circular pattern gives the highest capacitance density. The *bottom row* shows photographs of patterned films (Reprinted with permission from Macmillan Publishers Ltd: Nature Nanotechnology [62], copyright 2011)

off and assembled into a sandwich supercapacitor structure. They reported a surface area of 1,520 m^2/g and an electrical conductivity of 1,738 S/m [63]. The as-made devices can deliver a power density of ~20 W/cm^3, 20 times higher than that of activated-carbon-based EDLCs [63]. Later, the same group optimized their laser treating recipe and demonstrated hundreds of smaller supercapacitors produced on a single DVD disk within 30 min and power densities of ~200 W/cm^3, among the highest value achieved for supercapacitors then (Fig. 4.17) [64]. There are two notable aspects of their work worthy of a closer look. The first one is that the supercapacitors they demonstrated don't require any current collectors, as opposite to most of other reports on supercapacitors. This is mainly due to the high electrical conductivity measured for their laser-treated rGO samples. The second point is about the flexibility of their as-fabricated devices. These devices can be bent and twisted several times without any performance loss. These fascinating properties are definitely important breakthrough in supercapacitor research, and their products offered great feasibility to integrate with MEMS or CMOS in a single chip [64].

In 2013, Dan Li and coworkers in Monash University, Australia, made further improvements on rGO-based ultracapacitors [65, 69]. They successfully prepared rGO films with high ion-accessible surface area and low ion transport resistance, with the help of a capillary compression process in rGO-gel films in the presence of a nonvolatile liquid electrolyte. To be more specific, they followed their previous recipe to make rGO hydrogel films [69] with hydrazine reduction (Fig. 4.18). Then the films were soaked in a ratio-controlled volatile/nonvolatile miscible solutions,

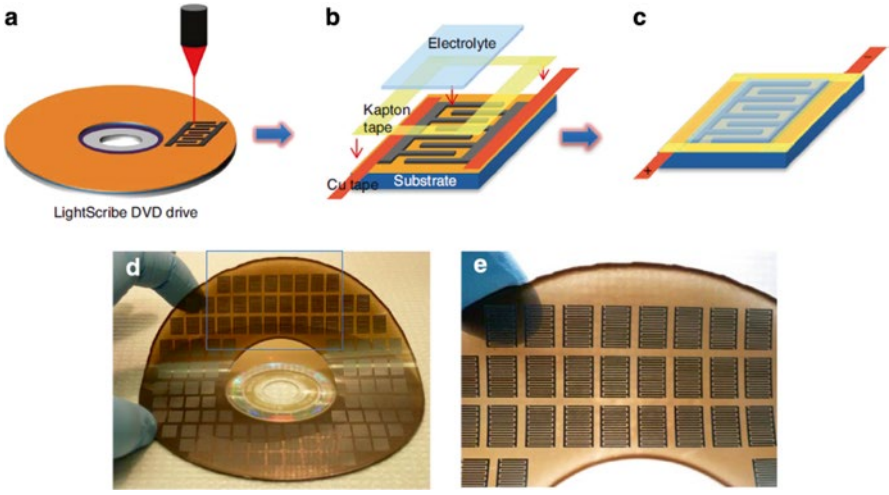

Fig. 4.17 Fabrication of LSG-MSL. (**a**–**c**) Schematic diagram showing the fabrication process for an LSG micro-supercapacitor. A GO film supported on a PET sheet is placed on a DVD media disk. The disk is inserted into a LightScribe DVD drive and a computer-designed circuit is etched onto the film. (**a**) The laser inside the drive converts the *golden-brown* GO into black LSG at precise locations to produce interdigitated graphene circuits. (**b**) Copper tape is applied along the edges to improve the electrical contacts, and the interdigitated area is defined by polyimide (Kapton) tape. (**c**) An electrolyte overcoat is then added to create a planar micro-supercapacitor. (**d**, **e**) This technique has the potential for the direct writing of micro-devices with high areal density. More than 100 micro-devices can be produced on a single run. The micro-devices are completely flexible and can be produced on virtually any substrate (Reprinted with permission from Macmillan Publishers Ltd: Nature Communications [64], copyright (2013))

stirred for 12 h to reach equilibrium. Deionized water was used as the volatile liquids, whereas sulfuric acid and an ionic liquid were used as two nonvolatile liquids. When they had a solvent-exchanged rGO hydrogel film, they placed it in a vacuum oven and the volatile liquid was removed under high vacuum (10 Pa). The evaporation of water exerted capillary compression between rGO layers and led to shrinkage of the thickness and increase of packing density. Superior volumetric energy density (59.9 Wh/L) and power density (8.6 kW/L) were achieved in their devices, mainly due to the much higher packing density of their electrode–electrolyte system. The key feature of their system is that the preincorporation of electrolytes in the rGO films ensured excellent rate performance of their supercapacitors.

In summary, rGO-based EDLCs are of great importance to both scientific and technological communities. Major breakthroughs have been demonstrated in the past 5 years; however, the biggest issues in EDLC research remain to be unsolved. For example, the energy density of EDLCs is still lower than the widely used lithium-ion batteries in the market. Furthermore, few researchers have investigated the self-discharge processes in supercapacitors, which are known to be orders of magnitude faster than that in batteries. To make ultracapacitors competitive alternatives to batteries, these technological issues will have to be addressed.

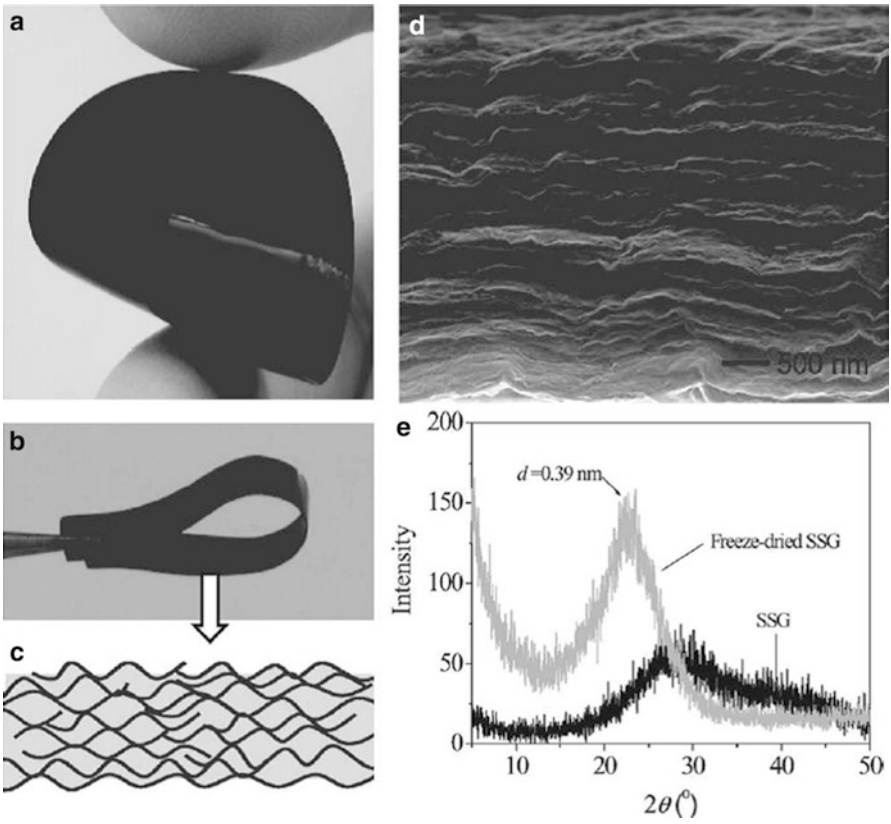

Fig. 4.18 Structure of the SSG film. (**a**, **b**) Photographs of the as-formed flexible SSG films. (**c**) Schematic of the cross section of the SSG film. (**d**) SEM image of the cross section of a freeze-dried SSG film. Given that the undried SSG film must be much more porous than shown in this SEM image. (**e**) XRD patterns of as-prepared and freeze-dried SSG films. The broad diffraction peak of the wet SSG film (from 27.9 to 44.8°) is likely due to the water confined in the CCG network because the corresponding d-spacing is less than the $d_{(002)}$ of graphite. Further experiments are required to understand the structure of the water in this SSG film (Reprinted with permission from Ref [69], copyright (2011) John Wiley & Sons, Inc.)

4.3 GO/rGO Anodes in Li-Ion Batteries

Today, Li-ion batteries (LIBs) have become the most promising energy storage technologies for portable electronics and transportation. However, the energy density of current batteries is still not enough to provide required energy after a single charge. The challenges are related to insufficient capacity and power density of electrodes as well as high cost and serious safety issue. In order to overcome these limitations, advanced electrode materials are required. Current LIBs use layered graphite materials as anodes, capable of storing ions in the material's bulk, but

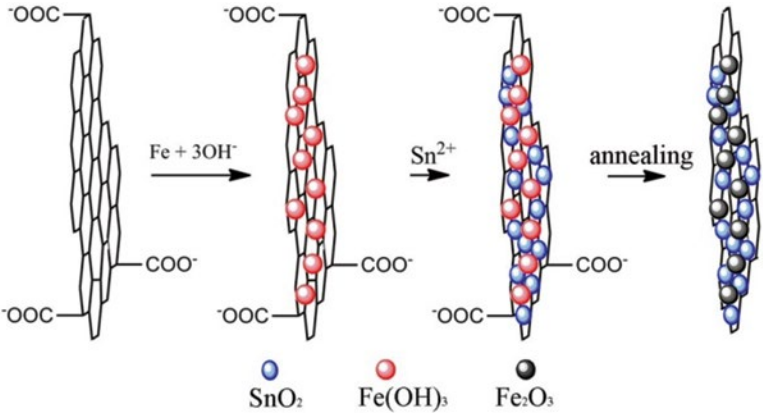

Fig. 4.19 Scheme of preparation of ternary rGO/Fe_2O_3/SnO_2nanocompoiste. Reprinted with permission from Ref. [93]. Copyright (2013) American Chemical Society

suffer from low energy and power density. The graphite anode can only intercalate one Li atom per six carbon atoms (LiC_6) with a theoretical capacity of 372 $mAhg^{-1}$ [70]. New anode materials with fast electron transport, large capacity, and efficient lithium-ion diffusion will lead to high-power and high-rate LIBs [71–74]. Thus, attention on the anode has been shifting from traditional graphite to other advanced materials with an aim to increase the number of lithiation sites and improve the diffusivity of Li [75–78].

Graphene materials, possessing high electron conductivity, large specific surface area (up to 2,600 m^2/g), and a broad window of electrochemical stability, hold great promise as an advanced material for energy storage technologies [21, 79–81]. The specific capacity of graphene for Li can be substantially higher than that of graphite, because graphene can adsorb lithium on both sides. Furthermore, the single layer of graphene provides a facile route for the diffusion of lithium ions, since the space for lithium intercalation is much larger than that in graphite interlayers [81–84]. Despite these advantages, graphene anodes experience significant irreversible capacity losses during charge/discharge cycling, mainly due to the restacking of graphene layers [85]. Recently, it was found that this problem can be alleviated by incorporating solid nanoparticles (e.g., Si, CuO, Fe_2O_3, SnO_2 Co_3O_4, or Mn_3O_4) in between the sheets to reduce the restacking degree [86–92]. Here, only one example is given based on our own research.

Recently, we proposed a novel approach to designing and synthesizing a ternary rGO/Fe_2O_3/SnO_2 graphene nanocomposite consisting of rGO with incorporation of highly Li active Fe_2O_3 and SnO_2 particles [93]. As shown in Fig. 4.19 [93], the rGO/Fe_2O_3/SnO_2 ternary nanocomposite was synthesized via an in situ precipitation of Fe_2O_3 nanoparticles using $FeCl_3$ precursor onto GO, followed by a subsequent reduction with $SnCl_2$ to obtain highly conductive rGO.

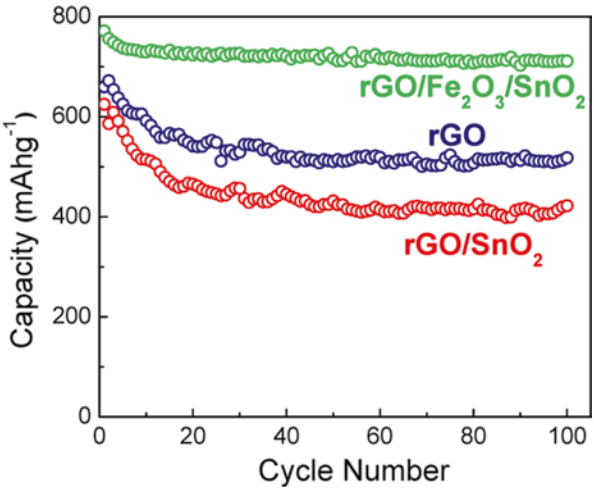

Fig. 4.20 A comparison of discharge–charge capacity measured with rGO, rGO/SnO_2, and rGO/Fe_2O_3/SnO_2 anodes up to 100 cycles. Reprinted with permission from Ref. [93]. Copyright (2013) American Chemical Society

Typically, GO aqueous solution was prepared through a modified Hummers method by using natural graphite powder as a precursor [94, 95]. In a typical synthesis procedure, $FeCl_3 \cdot 6H_2O$ (0.8 g) and urea (1.5 g) were added to 150 mL of GO solution (containing about 0.12 g GO) under constant stirring. After sonicating for 30 min, the suspension was transferred to a Teflon-lined autoclave and maintained at 120 °C for 4 h. Because the oxygen functional groups on the GO sheets can chemically bond with the metals ions, Fe^{3+} ions were likely anchored on the planes of the GO sheets [96]. Therefore, Fe^{3+} can be precipitated by OH^- on GO sheets when the urea decomposes during the hydrothermal process. In order to realize the reduction of GO, the suspension was adjusted to pH = 7.0 after cooling to room temperature. Then, $SnCl_2 \cdot H_2O$ was introduced into the above solution and a temperature of 30 °C was maintained for 1.0 h with continuous magnetic stirring to achieve a maximum reduction efficiency. The resulting precipitation was washed with water and ethanol several times during the centrifuge separation process.

As shown in Fig. 4.20 [93], the ternary anode material is superior to rGO and binary rGO/SnO_2 anodes, showing improved cycle stability and specific capacity. After 100 cycles, the charge capacities measured with the rGO/Fe_2O_3/SnO_2 anode are the highest relative to those of rGO and rGO/SnO_2, retaining a specific capacity of above 700 $mAhg^{-1}$ which can be retained during the subsequent 100 cycles. In the rGO-based ternary anode materials, rGO, Fe_2O_3, and SnO_2 particles play different but complementary roles. rGO serves as a matrix enabling both lithium ions and electrons to migrate to active sites, thereby fully maximizing the energy density offered by both graphene and Fe_2O_3. The rGO also is an effective elastic buffer to relieve the strain that would otherwise accumulate in the agglomerated Fe_2O_3 particles during Li uptake/release.

In turn, the dispersion of Fe_2O_3 and SnO_2particles on graphene prevents the restacking of graphene sheets, maintaining a high storage capacity of lithium during cycling. It is worth noting that the rGO used in this work is prepared via reduction of GO by $SnCl_2$, a nontoxic reducing agent, introducing SnO_2 in the same step. However, both the lithium insertion and extraction potentials of SnO_2 are below 0.7 V and just beyond the active potential range of Fe_2O_3 (0.7–2.0 V). Thus, due to the discrepancy in electrochemical active potentials, SnO_2 is expected to mainly serve as an inert matrix for Fe_2O_3 particles and keep them from agglomerating. This might be an important reason for the high performance observed from the graphene nanocomposite anode during the discharge–charge cycling.

Future research of rGO-based anodes will focus on (1) gaining a fundamental understanding of lithium-ion adsorption/desorption and diffusion kinetics in heteroatom-doped graphene structures using the proposed model systems and density functional theory (DFT) calculations, (2) exploring the facilitating roles of graphene and Si particles and their possible synergistic effects in developed composite anode materials, and (3) designing and synthesizing graphene-based composites with controllable morphology and structure for advanced lithium battery anodes. The cost-effective and functional rGO-based anodes will substantially improve Li^+-specific capacity, mass transport, and charge/discharge cyclic stability for next-generation LIBs.

4.4 Summary and Perspective

In the past decade, GOs or rGOs have emerged as important energy materials for electrochemical energy storages and conversion technologies, including fuel cells, metal–air batteries, supercapacitors, and lithium-ion batteries. Due to unique properties of rGO including high surface area, excellent electrical conductivity, good electrochemical stability, and easy functionalization of two-dimensional planes, superior performance was universally achieved on these graphene-based catalysts or electrode materials for these electrochemical devices. In this chapter, applications of GO/rGO-based materials were selectively reviewed in terms of their use as nonprecious metal catalysts in fuel cells and metal–air batteries and as high-performance electrodes in supercapacitors and lithium-ion batteries. The purpose is to highlight the comparisons among material synthesis, processing, structures, and properties.

Generally, during the synthesis of rGO, graphite precursors, reducing agents, and methods are critical to resulting morphologies and structures of rGO. Furthermore, the surface areas, porosity, defects, dopants, and reduction degree of rGO can directly link to corresponding material performance. Among studied methods to modify rGO, heteroatom doping is very effective to tune the structural and electronic properties of carbon planes in rGO, creating more active species for associated electrochemical reactions in various applications. In addition, development of rGO nanocomposites by integrating with nanoparticles and functional polymers will result in possible synergistic effects and further resolve the current problems of

rGO materials, thereby significantly enhancing performance metrics. Importantly, understanding the nature of active site or adsorption sites in these rGO materials and the associated reaction mechanism will further provide insights to rational design and synthesis of advanced rGO materials.

Acknowledgements G. W. acknowledges the support from the start-up funding of University at Buffalo, The State University of New York.

W. G. sincerely thank for the start-up funding support from the Department of Textile Engineering, Chemistry and Science at North Carolina State University, Raleigh, NC.

References

1. Abraham KM, Jiang Z (1996) A polymer electrolyte-based rechargeable lithium/oxygen battery. J Electrochem Soc 143:1–5
2. Van Mierlo J, Maggetto G (2007) Fuel cell or battery: electric cars are the future. Fuel Cells 7:165–173
3. Girishkumar G, McCloskey B, Luntz AC, Swanson S, Wilcke W (2010) Lithium–air battery: promise and challenges. J Phys Chem Lett 1:2193–2203
4. Debart A, Paterson AJ, Bao J, Bruce PG (2008) Alpha-MnO_2 nanowires: a catalyst for the O_2 electrode in rechargeable lithium batteries. Angew Chem Int Ed 47:4521–4524
5. Wu G, Zelenay P (2013) Nanostructured nonprecious metal catalysts for oxygen reduction reaction. Acc Chem Res 46:1878–1889
6. Li Q, Cao R, Chol J, Wu G (2014) Nanocarbon electrocatalysts for oxygen reduction in alkaline media for advanced energy conversion and storage. Adv Energy Mater 4:1301415
7. Li Q, Cao R, Cho J, Wu G (2014) Nanostructured carbon-based cathode catalysts for nonaqueous lithium-oxygen batteries. Phys Chem Chem Phys 16:13568–13582
8. Calle-Vallejo F, Martinez JI, Rossmeisl J (2011) Density functional studies of functionalized graphitic materials with late transition metals for oxygen reduction reactions. Phys Chem Chem Phys 13:15639–15643
9. Parvez K, Yang SB, Hernandez Y, Winter A, Turchanin A, Feng XL, Mullen K (2012) Nitrogen-doped graphene and its iron-based composite as efficient electrocatalysts for oxygen reduction reaction. ACS Nano 6:9541–9550
10. Wang H, Yang Y, Liang Y, Zheng G, Li Y, Cui Y, Dai H (2012) Rechargeable Li-O_2 batteries with a covalently coupled $MnCo_2O_4$-graphene hybrid as an oxygen cathode catalyst. Energy Environ Sci 5:7931–7935
11. Wu G, Nelson MA, Mack NH, Ma SG, Sekhar P, Garzon FH, Zelenay P (2010) Titanium dioxide-supported non-precious metal oxygen reduction electrocatalyst. Chem Commun 46:7489–7491
12. Wu G, More KL, Xu P, Wang H-L, Ferrandon M, Kropf AJ, Myers DJ, Ma S, Johnston CM, Zelenay P (2013) A carbon-nanotube-supported graphene-rich non-precious metal oxygen reduction catalyst with enhanced performance durability. Chem Commun 49:3291–3293
13. Zhang S, Dai LM (2013) Metal-free electrocatalysts for oxygen reduction. In: Shao M (ed) Electrocatalysis in fuel cells. Springer, London, pp 375–390
14. Gong KP, Du F, Xia ZH, Durstock M, Dai LM (2009) Nitrogen-doped carbon nanotube arrays with high electrocatalytic activity for oxygen reduction. Science 323:760–764
15. Qu LT, Liu Y, Baek JB, Dai LM (2010) Nitrogen-doped graphene as efficient metal-free electrocatalyst for oxygen reduction in fuel cells. ACS Nano 4:1321–1326
16. Yeager E (1984) Electrocatalysts for O_2 reduction. Electrochim Acta 29:1527–1537
17. Wu G, More KL, Johnston CM, Zelenay P (2011) High-performance electrocatalysts for oxygen reduction derived from polyaniline, iron, and cobalt. Science 332:443–447

18. Wu G, Li DY, Dai CS, Wang DL, Li N (2008) Well-dispersed high-loading Pt nanoparticles supported by shell-core nanostructured carbon for methanol electrooxidation. Langmuir 24:3566–3575
19. Pels JR, Kapteijn F, Moulijn JA, Zhu Q, Thomas KM (1995) Evolution of nitrogen functionalities in carbonaceous materials during pyrolysis. Carbon 33:1641–1653
20. Wu G, Dai C, Wang D, Li D, Li N (2010) Nitrogen-doped magnetic onion-like carbon as support for Pt particles in a hybrid cathode catalyst for fuel cells. J Mater Chem 20:3059–3068
21. Wu G, Mack NH, Gao W, Ma S, Zhong R, Han J, Baldwin JK, Zelenay P (2012) Nitrogen-doped graphene-rich catalysts derived from heteroatom polymers for oxygen reduction in non-aqueous lithium–O_2 battery cathodes. ACS Nano 6:9764–9776
22. Wu G, Swaidan R, Li D, Li N (2008) Enhanced methanol electro-oxidation activity of PtRu catalysts supported on heteroatom-doped carbon. Electrochim Acta 53:7622–7629
23. Sidik RA, Anderson AB, Subramanian NP, Kumaraguru SP, Popov BN (2006) O_2 reduction on graphite and nitrogen-doped graphite: experiment and theory. J Phys Chem B 110:1787–1793
24. Kim H, Lee K, Woo SI, Jung Y (2011) On the mechanism of enhanced oxygen reduction reaction in nitrogen-doped graphene nanoribbons. Phys Chem Chem Phys 13:17505–17510
25. Li XL, Wang HL, Robinson JT, Sanchez H, Diankov G, Dai HJ (2009) Simultaneous nitrogen doping and reduction of graphene oxide. J Am Chem Soc 131:15939–15944
26. Geng DS, Chen Y, Chen YG, Li YL, Li RY, Sun XL, Ye SY, Knights S (2011) High oxygen-reduction activity and durability of nitrogen-doped graphene. Energy Environ Sci 4:760–764
27. Li N, Wang ZY, Zhao KK, Shi ZJ, Gu ZN, Xu SK (2010) Synthesis of single-wall carbon nanohorns by arc-discharge in air and their formation mechanism. Carbon 48:1580–1585
28. Panchokarla LS, Subrahmanyam KS, Saha SK, Govindaraj A, Krishnamurthy HR, Waghmare UV, Rao CNR (2009) Synthesis, structure, and properties of boron- and nitrogen-doped graphene. Adv Mater 21:4726–4730
29. Shao YY, Zhang S, Engelhard MH, Li GS, Shao GC, Wang Y, Liu J, Aksay IA, Lin YH (2010) Nitrogen-doped graphene and its electrochemical applications. J Mater Chem 20:7491–7496
30. Jeong HM, Lee JW, Shin WH, Choi YJ, Shin HJ, Kang JK, Choi JW (2011) Nitrogen-doped graphene for high-performance ultracapacitors and the importance of nitrogen-doped sites at basal planes. Nano Lett 11:2472–2477
31. Liang YY, Li YG, Wang HL, Zhou JG, Wang J, Regier T, Dai HJ (2011) Co_3O_4 nanocrystals on graphene as a synergistic catalyst for oxygen reduction reaction. Nat Mater 10:780–786
32. Sheng ZH, Shao L, Chen JJ, Bao WJ, Wang FB, Xia XH (2011) Catalyst-Free synthesis of nitrogen-doped graphene via thermal annealing graphite oxide with melamine and its excellent electrocatalysis. ACS Nano 5:4350–4358
33. Lai L, Potts JR, Zhan D, Wang L, Poh CK, Tang C, Gong H, Shen Z, Lin J, Ruoff RS (2012) Exploration of the active center structure of nitrogen-doped graphene-based catalysts for oxygen reduction reaction. Energy Environ Sci 5:7936–7942
34. Sun B, Wang B, Su DW, Xiao LD, Ahn H, Wang GX (2012) Graphene nanosheets as cathode catalysts for lithium-air batteries with an enhanced electrochemical performance. Carbon 50:727–733
35. Xiao J, Mei D, Li X, Xu W, Wang D, Graff GL, Bennett WD, Nie Z, Saraf LV, Aksay IA, Liu J, Zhang J-G (2011) Hierarchically porous graphene as a lithium–air battery electrode. Nano Lett 11:5071–5078
36. Seredych M, Bandosz TJ (2014) Confined space reduced graphite oxide doped with sulfur as metal-free oxygen reduction catalyst. Carbon 66:227–233
37. Liang J, Jiao Y, Jaroniec M, Qiao SZ (2012) Sulfur and nitrogen dual-doped mesoporous graphene electrocatalyst for oxygen reduction with synergistically enhanced performance. Angew Chem Int Ed 51:11496–11500
38. Yang Z, Yao Z, Li G, Fang G, Nie H, Liu Z, Zhou X, Chen XA, Huang S (2011) Sulfur-doped graphene as an efficient metal-free cathode catalyst for oxygen reduction. ACS Nano 6:205–211
39. Wang SY, Iyyamperumal E, Roy A, Xue YH, Yu DS, Dai LM (2011) Vertically aligned BCN nanotubes as efficient metal-free electrocatalysts for the oxygen reduction reaction: a synergetic effect by co-doping with boron and nitrogen. Angew Chem Int Ed 50:11756–11760

40. Sheng Z-H, Gao H-L, Bao W-J, Wang F-B, Xia X-H (2012) Synthesis of boron doped graphene for oxygen reduction reaction in fuel cells. J Mater Chem 22:390–395
41. Byon HR, Suntivich J, Shao-Horn Y (2011) Graphene-based non-noble-metal catalysts for oxygen reduction reaction in acid. Chem Mater 23:3421–3428
42. Liang YY, Wang HL, Zhou JG, Li YG, Wang J, Regier T, Dai HJ (2012) Covalent hybrid of spinel manganese-cobalt oxide and graphene as advanced oxygen reduction electrocatalysts. J Am Chem Soc 134:3517–3523
43. Wu G, Li N, Zhou D-R, Mitsuo K, Xu B-Q (2004) Anodically electrodeposited Co + Ni mixed oxide electrode: preparation and electrocatalytic activity for oxygen evolution in alkaline media. J Solid State Chem 177:3682–3692
44. Wang HL, Liang YY, Li YG, Dai HJ (2011) Co1-xS-graphene hybrid: a high-performance metal chalcogenide electrocatalyst for oxygen reduction. Angew Chem Int Ed 50: 10969–10972
45. Yan XY, Tong XL, Zhang YF, Han XD, Wang YY, Jin GQ, Qin Y, Guo XY (2012) Cuprous oxide nanoparticles dispersed on reduced graphene oxide as an efficient electrocatalyst for oxygen reduction reaction. Chem Commun 48:1892–1894
46. Li Q, Xu P, Zhang B, Tsai H, Zheng S, Wu G, Wang H-L (2013) Structure-dependent electrocatalytic properties of Cu_2O nanocrystals for oxygen reduction reaction. J Phys Chem C 117:13872
47. Wu ZS, Yang SB, Sun Y, Parvez K, Feng XL, Mullen K (2012) 3D Nitrogen-doped graphene aerogel-supported Fe_3O_4 nanoparticles as efficient eletrocatalysts for the oxygen reduction reaction. J Am Chem Soc 134:9082–9085
48. He Q, Li Q, Khene S, Ren X, López-Suárez FE, Lozano-Castello D, Bueno-López A, Wu G (2013) High-loading cobalt oxide coupled with nitrogen-doped graphene for oxygen-reduction in anion-exchange membrane alkaline fuel cells. J Phys Chem C 117:8697–8707
49. Lee J-S, Tai Kim S, Cao R, Choi N-S, Liu M, Lee KT, Cho J (2011) Metal–air batteries with high energy density: Li–Air versus Zn–Air. Adv Energy Mater 1:34–50
50. Cheng F, Chen J (2012) Metal-air batteries: from oxygen reduction electrochemistry to cathode catalysts. Chem Soc Rev 41:2172–2192
51. Trahey L, Johnson CS, Vaughey JT, Kang S-H, Hardwick LJ, Freunberger SA, Bruce PG, Thackeray MM (2011) Activated lithium-metal-oxides as catalytic electrodes for Li–O_2 cells. Electrochem Solid State Lett 14:A64–A66
52. Zhao Y, Xu L, Mai L, Han C, An Q, Xu X, Liu X, Zhang Q (2012) Hierarchical mesoporous perovskite La0.5Sr0.5CoO_2.91 nanowires with ultrahigh capacity for Li-air batteries. Proc Natl Acad Sci U S A 109:19569–19574
53. Oh SH, Nazar LF (2012) Oxide catalysts for rechargeable high-capacity Li–O_2 batteries. Adv Energy Mater 2:903–910
54. Grimaud A, Carlton CE, Risch M, Hong WT, May KJ, Shao-Horn Y (2013) Oxygen evolution activity and stability of $Ba_6Mn_5O_{16}$, $Sr_4Mn_2CoO_9$, and Sr6Co5O15: the influence of transition metal coordination. J Phys Chem C 117:25926–25932
55. Jung KN, Lee JI, Im WB, Yoon S, Shin KH, Lee JW (2012) Promoting Li_2O_2 oxidation by an La(1.7)Ca(0.3)Ni(0.75)Cu(0.25)O_4 layered perovskite in lithium-oxygen batteries. Chem Commun (Camb) 48(75):9406–9408
56. Shao YY, Ding F, Xiao J, Zhang J, Xu W, Park S, Zhang JG, Wang Y, Liu J (2013) Making Li-air batteries rechargeable: material challenges. Adv Funct Mater 23:987–1004
57. Cao R, Lee JS, Liu ML, Cho J (2012) Recent Progress in non-precious catalysts for metal-air batteries. Adv Energy Mater 2:816–829
58. Wang HL, Yang Y, Liang YY, Zheng GY, Li YG, Cui Y, Dai HJ (2012) Rechargeable Li-O_2 batteries with a covalently coupled $MnCo_2O_4$-graphene hybrid as an oxygen cathode catalyst. Energy Environ Sci 5:7931–7935
59. Wang H, Dai H (2013) Strongly coupled inorganic-nano-carbon hybrid materials for energy storage. Chem Soc Rev 42:3088–3113
60. Stoller MD, Park S, Zhu Y, An J, Ruoff RS (2008) Graphene-based ultracapacitors. Nano Lett 8:3498–3502

61. Zhu Y, Murali S, Stoller MD, Ganesh K, Cai W, Ferreira PJ, Pirkle A, Wallace RM, Cychosz KA, Thommes M (2011) Carbon-based supercapacitors produced by activation of graphene. Science 332:1537–1541
62. Gao W, Singh N, Song L, Liu Z, Reddy ALM, Ci L, Vajtai R, Zhang Q, Wei B, Ajayan PM (2011) Direct laser writing of micro-supercapacitors on hydrated graphite oxide films. Nat Nanotechnol 6:496–500
63. El-Kady MF, Strong V, Dubin S, Kaner RB (2012) Laser scribing of high-performance and flexible graphene-based electrochemical capacitors. Science 335:1326–1330
64. El-Kady MF, Kaner RB (2013) Scalable fabrication of high-power graphene micro-supercapacitors for flexible and on-chip energy storage. Nat Commun 4:1475
65. Yang X, Cheng C, Wang Y, Qiu L, Li D (2013) Liquid-mediated dense integration of graphene materials for compact capacitive energy storage. Science 341:534–537
66. Namisnyk AM (2003) A survey of electrochemical supercapacitor technology. University of Technology, Sydney
67. Reddy ALM, Ramaprabhu S (2007) Nanocrystalline metal oxides dispersed multiwalled carbon nanotubes as supercapacitor electrodes. J Phys Chem C 111:7727–7734
68. Gao W, Wu G, Janicke MT, Cullen DA, Mukundan R, Baldwin JK, Brosha EL, Galande C, Ajayan PM, More KL, Dattelbaum AM, Zelenay P (2014) Ozonated Graphene Oxide Film as a Proton-Exchange Membrane. Angew Chem Int Ed 53:3588–3593
69. Yang X, Zhu J, Qiu L, Li D (2011) Bioinspired effective prevention of restacking in multilayered graphene films: towards the next generation of high-performance supercapacitors. Adv Mater 23:2833–2838
70. Dahn JR, Zheng T, Liu Y, Xue JS (1995) Mechanisms for lithium insertion in carbonaceous materials. Science 270:590–593
71. Chan CK, Peng H, Liu G, McIlwrath K, Zhang XF, Huggins RA, Cui Y (2008) High-performance lithium battery anodes using silicon nanowires. Nat Nanotechnol 3:31–35
72. Armand M, Tarascon JM (2008) Building better batteries. Nature 451:652–657
73. Chen Z, Dai C, Wu G, Nelson M, Hu X, Zhang R, Liu J, Xia J (2010) High performance $Li_3V_2(PO_4)_3$/C composite cathode material for lithium ion batteries studied in pilot scale test. Electrochim Acta 55:8595–8599
74. Xu X, Cao R, Jeong S, Cho J (2012) Spindle-like mesoporous α-Fe_2O_3 anode material prepared from MOF template for high-rate lithium batteries. Nano Lett 12:4988–4991
75. Han F-D, Bai Y-J, Liu R, Yao B, Qi Y-X, Lun N, Zhang J-X (2011) Template-free synthesis of interconnected hollow carbon nanospheres for high-performance anode material in lithium-ion batteries. Adv Energy Mater 1:798–801
76. Chan CK, Patel RN, O'Connell MJ, Korgel BA, Cui Y (2010) Solution-grown silicon nanowires for lithium-ion battery anodes. ACS Nano 4:1443–1450
77. Zhu X, Zhu Y, Murali S, Stoller MD, Ruoff RS (2011) Nanostructured reduced graphene oxide/Fe_2O_3 composite as a high-performance anode material for lithium ion batteries. ACS Nano 5:3333–3338
78. Liu R, Li N, Xia G, Li D, Wang C, Xiao N, Tian D, Wu G (2013) Assembled hollow and core-shell SnO_2 microspheres as anode materials for Li-ion batteries. Mater Lett 93:243–246
79. Stankovich S, Dikin DA, Dommett GHB, Kohlhaas KM, Zimney EJ, Stach EA, Piner RD, Nguyen ST, Ruoff RS (2006) Graphene-based composite materials. Nature 442:282–286
80. Yoo E, Kim J, Hosono E, Zhou H-S, Kudo T, Honma I (2008) Large reversible Li storage of graphene nanosheet families for use in rechargeable lithium ion batteries. Nano Lett 8:2277–2282
81. Wang C, Li D, Too CO, Wallace GG (2009) Electrochemical properties of graphene paper electrodes used in lithium batteries. Chem Mater 21:2604–2606
82. Lian P, Zhu X, Liang S, Li Z, Yang W, Wang H (2010) Large reversible capacity of high quality graphene sheets as an anode material for lithium-ion batteries. Electrochim Acta 55:3909–3914
83. Wang G, Shen X, Yao J, Park J (2009) Graphene nanosheets for enhanced lithium storage in lithium ion batteries. Carbon 2049–2053:47

84. Wu Z-S, Ren W, Xu L, Li F, Cheng H-M (2011) Doped Graphene Sheets As Anode Materials with Superhigh Rate and Large Capacity for Lithium Ion Batteries. ACS Nano 5:5463–5471
85. Evanoff K, Magasinski A, Yang J, Yushin G (2011) Nanosilicon-Coated Graphene Granules as Anodes for Li-Ion Batteries. Adv Energy Mater 1:495–498
86. Wang H, Cui L-F, Yang Y, Sanchez Casalongue H, Robinson JT, Liang Y, Cui Y, Dai H (2010) Mn_3O_4-graphene hybrid as a high-capacity anode material for lithium ion batteries. J Am Chem Soc 132:13978–13980
87. Yang S, Feng X, Ivanovici S, Müllen K (2010) Fabrication of graphene-encapsulated oxide nanoparticles: towards high-performance anode materials for lithium storage. Angew Chem Int Ed Engl 49:8408–8411
88. Zhou G, Wang D-W, Li F, Zhang L, Li N, Wu Z-S, Wen L, Lu GQ, Cheng H-M (2010) Graphene-wrapped Fe_3O_4 anode material with improved reversible capacity and cyclic stability for lithium ion batteries. Chem Mater 22:5306–5313
89. Wu Z-S, Ren W, Wen L, Gao L, Zhao J, Chen Z, Zhou G, Li F, Cheng H-M (2010) Graphene anchored with Co_3O_4 nanoparticles as anode of lithium ion batteries with enhanced reversible capacity and cyclic performance. ACS Nano 4:3187–3194
90. Wang JZ, Zhong C, Wexler D, Idris NH, Wang ZX, Chen LQ, Liu HK (2011) Graphene-encapsulated Fe_3O_4 nanoparticles with 3D laminated structure as superior anode in lithium ion batteries. Chemistry 17:661–667
91. Zhang L-S, Jiang L-Y, Yan H-J, Wang WD, Wang W, Song W-G, Guo Y-G, Wan L-J (2010) Mono dispersed SnO_2 nanoparticles on both sides of single layer graphene sheets as anode materials in Li-ion batteries. J Mater Chem 20:5462–5467
92. Li B, Cao H, Shao J, Li G, Qu M, Yin G (2011) Co_3O_4@ graphene composites as anode materials for high-performance lithium ion batteries. Inorg Chem 50:1628–1632
93. Xia G, Li N, Li D, Liu R, Wang C, Li Q, Lu X, Spendelow J, Zhang J, Wu G (2013) Graphene/Fe_2O_3/SnO_2/ternary nanocomposites as a high-performance anode for lithium ion batteries. ACS Appl Mater Interfaces 5:8607–8614
94. Hummers WS, Offeman RE (1958) Preparation of Graphitic Oxide. J Am Chem Soc 80:1339
95. Marcano DC, Kosynkin DV, Berlin JM, Sinitskii A, Sun Z, Slesarev A, Alemany LB, Lu W, Tour JM (2010) Improved Synthesis of Graphene Oxide. ACS Nano 4:4806–4814
96. Ramesha GK, Sampath S (2009) Electrochemical reduction of oriented graphene oxide films: an in situ Raman spectroelectrochemical study. J Phys Chem C 113:7985–7989